Cloud Cameras at the Pierre Auger Observatory

BY

Michael G. Winnick, BSc (Hons)

A dissertation submitted

In partial fulfillment of the requirements for the degree of

Doctor of Philosophy

University of Adelaide

School of Chemistry and Physics

June 2010

Chapter 1

Cosmic rays

Cosmic rays, highly energetic charged particles of extraterrestial origin, were first discovered by Victor Hess in 1912 [98]. Low energy ($< 10^{14}$ eV) cosmic ray particles have been well studied in the past by both satellite and balloon-borne detectors and are thought to originate from within our local Milky Way galaxy. At higher energies, the observing technique is to study the cascades of particles produced through interactions with our atmosphere called extensive air showers.

The flux of cosmic rays decreases with energy E, roughly as $E^{-2.7}$ which means that conclusions about their origin and acceleration become increasingly difficult at higher energies. Measurements of the cosmic ray mass composition may reveal hints about their origin but these too are uncertain at higher energies because of the low flux of particles. There are a number of theoretical mechanisms to explain the acceleration of low energy cosmic rays but a great deal of mystery remains about the origin of their higher energy ($> 10^{18}$ eV) cousins. Within this chapter a brief summary of cosmic rays, their composition, flux and possible origins, will be given.

1.1   History

Cosmic ray particles were first recognized early in the 20th century. Originally they were believed to be some sort of radiation originating from the Earth. It wasn't until later that people realized that they were in fact dealing with charged particles, and that these particles were the result of interactions initiated by energetic cosmic ray primary particles in the Earth's atmosphere.

In 1912, while studying the variation of atmospheric ionization with altitude, Victor Hess first discovered cosmic rays [98]. Atmospheric ionization had been thought to be the result of some sort of ambient radiation from the

Earth, therefore it was expected that atmospheric ionization would decrease with altitude. Hess tested this hypothesis by measuring atmospheric ionization at different altitudes using an electroscope on a balloon flight. He noted that while the degree of ionization decreased as expected for the first 700m above the Earth, it rapidly increased at higher altitudes. This trend was later independently confirmed by Kolhörster [116]. Hess drew the conclusion that atmospheric ionization was actually a result of some sort of extraterrestrial radiation bombarding the Earth [86]. At that time, γ-rays were understood to be the most penetrating form of radiation. It was therefore assumed that this mysterious radiation took the form of γ-rays, and thus were subsequently termed 'cosmic rays' in 1926 by Millikan.

When Clay studied the variation in cosmic ray intensity with latitude [58] in 1927, he noted that the flux was less in equatorial regions, relative to higher latitudes - an effect explained by studies of the passage of charged particles in the geomagnetic field. Subsequent studies found an excess of cosmic rays at westerly zenith angles [105][18]. These observations suggested that cosmic rays were predominantly positively charged particles as opposed to γ-rays. Further work [154] indicated that some negatively charged particles were also present.

The most important discovery in modern cosmic ray physics was made by Pierre Auger and his collaborators [25][26], when they discovered that particles were arriving in 'showers'. These cascades of particles were detected through coincident detections by three Geiger-Muller counters spaced some 300m apart. Auger thought that these showers were being initiated by highly energetic (10^{15}eV) electrons, positrons or γ-rays and could be explained by electromagnetic cascade theory. Later experiments showed this explanation to be incorrect however, as a significant muon component was being detected by experiments in the Alps [66][61] - an observation not expected to result just from a electron/photon cascade. Later measurements suggested that cosmic ray showers were likely being initiated by protons or nuclei [110].

The discovery of the existence of naturally occuring highly energetic particles excited much interest in the nature and origin of these particles. Due to their low flux it was impractical to attempt to measure them directly, therefore large collection areas were necessary to effectively study them. One of the first air shower surface detector arrays appeared in the late 1950's [55] at the Harvard College Observatory, and consisted of an array of 1m^2 plastic scintillators. These scintillators were placed in a circular arrangement and demonstrated that it was possible to infer the arrival direction and energy of air shower primary particles, using timing and particle density information respectively.

A larger array was soon built specifically to study cosmic rays showers with energy $> 10^{17}$eV at Volcano Ranch in New Mexico [124]. In 1962, this array detected a cosmic ray extensive air shower with an estimated initiating primary particle energy of 10^{20}eV [125]. This was an important observation, as due to the GZK (Greisen-Zatsepin-Kuzmin) effect [90][182] (described later) this particle must have originated within around only 50 megaparsecs of the Earth. The high energy and localized nature of these ultra high energy cosmic ray particles means that they would only be deflected by a few degrees by magnetic fields before arriving at the Earth, making them a useful tool in determining the origin of cosmic rays. This is especially likely if the primary particles have a low charge like protons.

To study the origin of ultra-high energy cosmic rays further (and to investigate the GZK effect) several large air shower detection experiments were developed. SUGAR (Sydney University Giant Airshower Recorder) [178] ran between 1968 to 1979, and covered an area of 70km^2 with 47 scintillator detectors that measured the muon content of incident air showers. The Yakutsk array [17] in Siberia covers an area of 10km^2 and uses plastic scintillator ground detectors, buried muon detectors and 50 atmospheric Cherenkov detectors to perform measurements of cosmic ray air showers. Another detector array (AGASA) [52] run by the University of Tokyo in Japan, studied showers with muon detectors and over 200 plastic scintillator surface detectors. The first fluorescence detector was developed at Dugway Proving Ground in the Utah desert and was called 'Fly's Eye' [49]. This detector studied extensive air showers through the fluorescence they produce while travelling through the Earth's atmosphere. The Fly's Eye was superseded in 1993 by the HiRes (High Resolution Fly's Eye) fluorescence detector.

The Pierre Auger Observatory was proposed in the 1990's as a large scale hybrid detector, studying cosmic ray air showers not only through their fluorescence, but also a large array of surface water Cherenkov detectors. The dual measurements afforded by using both instruments to measure a particular air shower allows different energy and arrival direction measurements to be compared and combined. This allows an improved resolution of air shower arrival directions to be achieved. The Southern Observatory located in Argentina has been completed and consists of a surface detector array spanning some 3000km^2, surrounded by four fluorescence detectors. A similar Northern Observatory in the United States is currently in the planning stage.

1.2   Anisotropy

Cosmic ray anisotropy is the search for a departure from isotropy in cosmic ray particle arrival directions. While travelling through the interstellar and intergalactic medium, cosmic rays will be deflected by magnetic fields they encounter. This deflection means that it is generally not possible to trace the arrival direction of cosmic rays back to their source, thus the arrival directions of such cosmic ray particles are generally expected to be isotropic. Ultra-high energy cosmic rays ($> 10^{18}$eV) are expected to be anisotropic if there exists only a small number of sources from which such particles orginate. Generally speaking, due to their deflection by magnetic fields, only ultra-high energy cosmic ray particles are expected to have arrival directions that roughly correspond to their actual direction of origin.

The deflection of cosmic rays between their origin and measurement on the Earth, depends upon their gyroradius while travelling through any magnetic fields encountered. Cosmic rays are charged particles, therefore they have a gyroradius r_G (in parsecs) while travelling through a regular magnetic field - as seen in equation 1.1:

$$r_G = \frac{1.08 E_{PeV}}{ZB} \qquad (1.1)$$

where where B is the magnetic field strength in μG, Z is the atomic charge of the particle and E_{PeV} is the energy of the particle in units of 10^{15} eV.

If the gyroradius is too small, the cosmic ray particle will be significantly deflected from its original pointing direction and cannot be directly traced back to its origin upon measurement on Earth. Thus the ability to resolve a cosmic ray particle's origin depends upon how energetic it is, how strong the magnetic field it has travelled through is, how far it has travelled, and what charge it has.

Some measurements of the local galactic magnetic field [148][51] (via pulsar rotation measures) suggest a regular field strength along the galaxy's spiral arms of ∼2 μG and a randomly orientated field strength of ∼5 μG with a typical scale length of ∼ 100 parsecs. Low energy cosmic rays (with gyroradii << 100 pc) will be scattered by the galactic magnetic field before encountering the Earth. Successively higher energy ($> 10^{18}$ eV) cosmic rays however will suffer less deflection. A $> 10^{20}$ eV proton would be able to effectively traverse the galaxy with only a few degrees of deflection and retain useful directional information.

A common method of calculating cosmic ray anisotropy is to use a harmonic analysis of the right ascension of the cosmic ray arrival directions [126]. Anisotropy results often quote the amplitude of the first and second

NOTE:
This figure is included on page 5
of the print copy of the thesis held in
the University of Adelaide Library.

Table 1.1: *Table taken from [60]. First and second harmonics of the cosmic ray anisotropy in the energy range* $1 - 3x10^{15}$ *eV.*

harmonic along with the accompanying phase. Table 1.1 describes the harmonics of $1\text{-}3x10^{15}$ eV cosmic rays calculated by Clay *et al.* in 1998 [60] using data measured in both the Southern and Northern hemispheres. These results suggest an anisotropy, in right ascension, with an amplitude of order 0.2%. Other studies calculate an anisotropy of below 0.1% up to energies of 10^{14} eV, and below 10% at 10^{17} eV [127]. Anistropy is not observed experimentally (and not generally expected) for lower energy cosmic rays due to their low energy and subsequent small gyroradius (a proton with energy 10^{15} eV would have a gyroradius of only about 1pc in a $1\mu G$ magnetic field).

Some anisotropy ($\sim$0.6% [87]) is expected due to the 'Compton-Getting' effect [63], whereby extra cosmic rays should be observed coming from the direction of the Earth's net movement. While current experiments theoretically have enough sensitivity to detect this effect, it has thus far failed to be observed.

Measurements from AGASA have indicated a 4.5σ excess of cosmic rays in the $10^{18}\text{-}10^{18.4}$eV energy range coming from within 10° of the galactic centre [97], and a 3.9σ excess from the direction of the Cygnus region. This energy range was selected through a search for the energy range where the anisotropy was the greatest. A harmonic analysis for measured cosmic rays in this energy range, across the galactic plane, indicates an anisotropy of 4%.

An excess of cosmic rays arriving from the direction of the galactic center has also been measured through analysis of data recorded by SUGAR [38]. In the energy range $10^{17.9}\text{-}10^{18.5}$eV, within 7.5° of the galactic center, a marginally significant excess was measured. The probability that this excess was due to a statistical fluctuation is 0.005. The location of this excess is consistent with the AGASA result mentioned previously.

Due to their high energies, ultra-high energy (E $> 10^{19}$ eV) cosmic rays will have a relatively large gyroradius in all but the strongest magnetic fields, resulting in a small deflection between their origin and a detector on Earth. Recent results released by the Auger collaboration [10] (see chapter 2) have suggested a possible correlation between ultra-high energy cosmic rays (UHECR) and AGN (active galactic nuceli). This anistropy has more than a
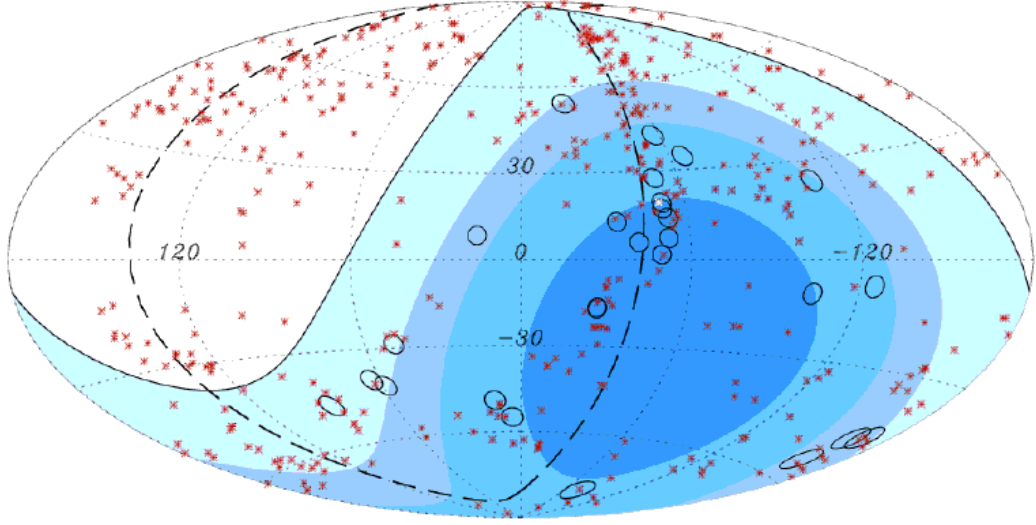
Figure 1.1: *Figure taken from [10]. Aitoff projection of the celestial sphere in galactic coordinates with circles of 3.2° centred at the arrival directions of 27 cosmic rays detected by the Pierre Auger Observatory with reconstructed energies E > 57 EeV. The positions of the 442 AGN (292 within the field of view of the Observatory) with redshift z≤0.017 (D < 71 Mpc) from [175] are indicated by asterisks. The solid line draws the border of the field of view for the Southern site of the observatory (with zenith angles smaller than 60°). The dashed line is, for reference, the super-galactic plane. Darker colour indicates larger relative exposure. Each coloured band has equal integrated exposure. Centaurus A, one of the closest AGN, is marked in white.*

99% confidence level, comparing 27 separate high energy (> 57 EeV)[1] cosmic ray events with a catalogue of some 442 AGN with redshifts (z< 0.017) - as seen in figure 1.1. This result supports the hypothesis that UHECRs are predominently protons as the angular scale of the correlation is only a few degrees (a heavier composition would suffer more deflection, and so result in a smaller anistropy) and of extra-galactic origin. This result does not definitely mean that UHECR come from AGN however, as other possible sources distributed like the AGN are also present. This result has yet to be confirmed by other independent measurements.

---

[1]1 EeV = 10^{18}eV

1.3 Energy spectrum

In this section the measured flux of cosmic rays will be discussed with respect to their energies.

Very low energy cosmic rays are difficult to measure due to deflection caused by the magnetic field of the solar wind. Higher energy measurements of the flux have been successively made however and reveal (for the most part) a spectrum well described by a power law. One interesting deviation from the power law occurs in the "knee" region around 4×10^{15} eV where the measured spectrum steepens - an effect for which several theoretical explanations exist. Another interesting deviation occurs at "ankle" region at 5×10^{18} eV, where the rate of the decrease of the flux slows down. At higher energies, beginning around 4×10^{19} eV, suppression of the cosmic ray flux is expected due to the GZK (Greisen-Zatsepin-Kuzmin) effect. Poor statistics of ultra-high energy cosmic rays have previously made this suppression difficult to confirm, but recent results from HiRes and the Pierre Auger Observatories are consistent with this effect. It remains to be seen however, if this is due to the GZK effect, or is associated with a cutoff in the spectrum intrinsic to the cosmic ray particle production source(s).

Measurement of very low energy (< 300 MeV) cosmic rays is complicated by a magnetic field created by the solar wind which acts to deflect such particles away from the inner solar system. The solar wind consists of a steady stream of magnetized plasma emitted by the sun in all directions, and effectively acts as a shield against protons with less than 300 MeV (or heavier nuclei with same energy to charge ratio). Higher energy particles that make it past the solar wind may be measured directly or indirectly by instruments on (or above) the Earth.

The measured flux of cosmic rays varies substantially with energy and the integral flux ranges from 0.1 particle m^{-2}sec^{-1} per steradian above 1 TeV, down to around 1 particle km^{-2}century^{-1} per steradian above 10^{20} eV. Many independent measurements of the flux have been made at lower energies (as seen in figure 1.2). Measurements at higher energies are much more uncertain due to the increased scarcity of particles. The cosmic ray (all particle) flux differential spectrum is well described by a piece-wise power law - decreasing as E$^{-2.7}$ up until the "knee" (at 4×10^{15} eV), then E$^{-3.1}$ up until the ankle at 4×10^{18} eV [165].

One possible explanation for the knee in the cosmic ray spectrum is the postulate that the propagation mechanism or source of cosmic rays is rigidity dependent [143]. The rigidity R of a relativistic cosmic ray is defined
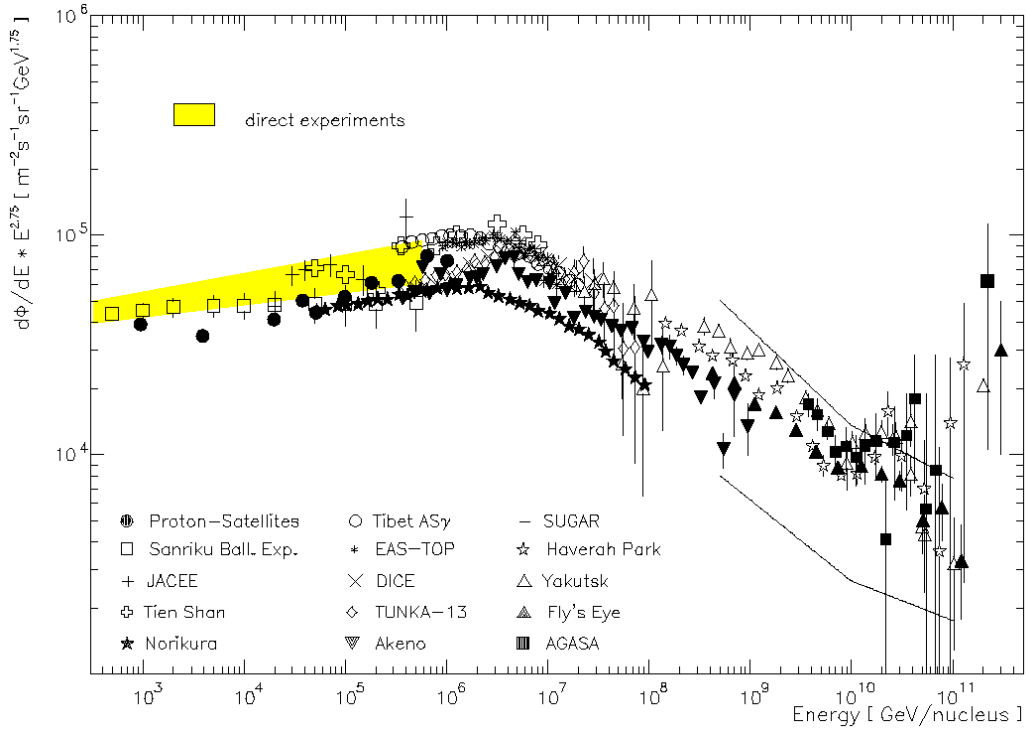
Figure 1.2: *Figure taken from [177]. The cosmic ray all particle spectrum observed by different experiments above 10^{11} eV. The differential flux was multiplied by $E^{2.75}$ to project out its steeply declining character. The "knee" may be observed at 4×10^{15} eV and the "ankle" at 5×10^{18} eV.*

in equation 1.2:

$$R = \frac{pc}{Z} \tag{1.2}$$

where p is the cosmic ray momentum, c is the speed of light and Z is the charge of the cosmic ray particle.

Cosmic rays of identical rigidity will have identical gyroradii in a particular magnetic field regardless of their energy. Cosmic rays can expect to leak out of a magnetic confinement region when they are accelerated to such an energy that their gyroradius is greater than the size of that region. Suppose protons leaked out of this region at some energy E (as this is the point where their gyroradii are large enough), then heavier nuclei are going to start leaking out at multiples of this energy e.g. $26E$ in the case of iron nuclei. Within the cosmic ray flux spectrum this effect would manifest as a series of bumps over a range of energies. Measurements recently made by KASCADE [20] support the idea of a rigidity dependent knee.
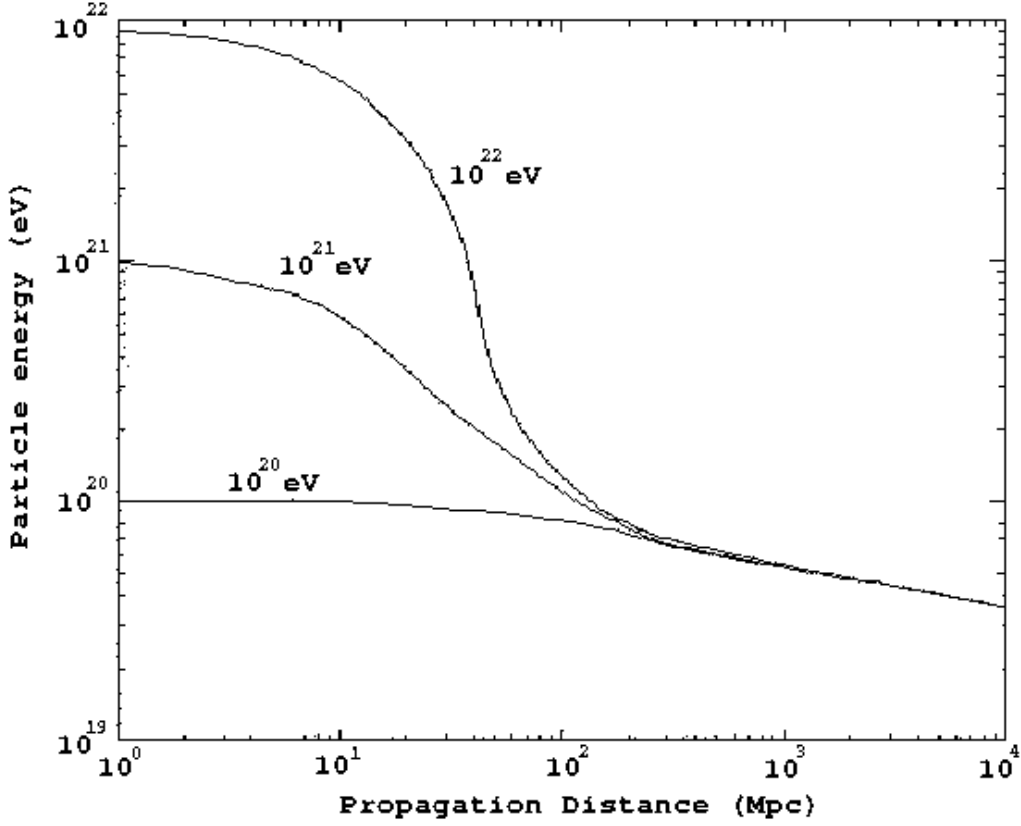
Figure 1.3: *Plot taken from [64]. Demonstrates the attenuation of energy due to the GZK effect as ultra-high energy protons propagate through space. Protons with initial energies 10^{20}, 10^{21} and 10^{22} eV are propagated through space, and their shift in energy due to the GZK effect plotted as a function of this propagation distance.*

At higher energies still, the cosmic ray flux of protons (seen in figure 1.2) above energies of $4x10^{19}$ eV is expected to be suppressed by the GZK effect [90][182]. Cosmic ray particles propagating through space at high energies above this will interact with microwave background radiation in a pion-photoproduction process demonstrated for protons in equation 1.3.

$$p + \gamma \longrightarrow p + \pi^{+}$$
$$p + \gamma \longrightarrow p + \pi^{0} \qquad (1.3)$$

Each interaction results in proton energy loss of approximately 20%. Thus any UHECRs produced will gradually have their energy degraded as they propagate through space. This attenuation is demonstrated in figure 1.3 where the estimated energies of three protons starting with energy 10^{20}, 10^{21}

and 10^{22} eV are plotted as a function of distance travelled. Note that higher energy particles lose energy faster than lower energy particles. Thus any UHECRs detected above 10^{20} eV must have their origin relatively close by (within 100 Mpc), otherwise their energy would have long since been lost.

Only relatively recently has the cosmic ray spectrum been measured thoroughly at energies above the ankle [13]. In figure 1.4 is presented the measured UHECR flux by the Pierre Auger Observatory. The ankle is clearly seen in the data at approximately $4x10^{18}$ eV, where the measured flux begins to vary approximately as $E^{-2.7}$ before steepening further above approximately $3x10^{19}$ eV. Also apparent is the flux suppression above $10^{19.6}$ eV predicted by the GZK effect [11].

NOTE:
This figure is included on page 10
of the print copy of the thesis held in
the University of Adelaide Library.

Figure 1.4: *Figure taken from [13]. The measured combined energy spectrum of cosmic ray particles by the Pierre Auger Observatory.*

1.4 Mass composition

The determination of the mass composition of cosmic rays is important in that it provides clues as to their origin and acceleration mechanism. Mass composition measurements at low energies ($< 10^{14}$ eV) are readily available through balloon and satellite observations. At these energies the composition has been determined to be primarily of a lighter or proton dominated composition. Measurements of the mass composition at higher energies, up to around 10^{15} eV start becoming more problematic due to the lower particle flux, though measurements indicate a trend towards a heavier composition. Cosmic ray particles above 10^{15} eV are nearly impossible to detect directly and must be studied through the extensive air showers they produce in the Earth's atmosphere.

At very low cosmic ray energies ($10^9 - 10^{11}$ eV), direct measurements of mass composition have been made. About 2% of the measured flux in this energy range takes the form of energetic electrons and positrons. The remaining 98% is in the form of hadronic nuclei, of which about 87% are hydrogen, 12% helium and the remaining 1% consisting of heavier nuclei [164]. Figure 1.5 shows the relative abundance of lower energy cosmic ray nuclei, with Z < 30. Nuclei with 30 <Z< 90 have been detected but are relatively insignificant, having an abundance of only 10^{-4} that of iron [79]. The spallation of C, N and O nuclei in the interstellar medium is thought to be the cause of the over-abundance of Li, Be and B compared with their respective local solar abundances. Spallation is the process by which nucleons are lost from a particular nucleus due to a collision. The abundance of Sc-Mn is also thought to be a result of spallation of iron nuclei.

Measurements of the mass composition of more energetic ($< 10^{15}$ eV) cosmic ray particles have been performed by the JACEE collaboration (Japanese-American-Emulsion-Chamber-Experiment) [23][24] using balloon borne emulsion chambers. Emulsion chambers have a series of 'target' lead plates with which any incident cosmic ray particles are prone to collide and interact with. This collision results in a shower of γ-rays and subatomic particles which continue down through several layers of emulsion plate and x-ray films, marking them in the process. These markings are then manually scanned and interpreted to reveal the characteristics of the interacting primary. Results from this experiment indicate that the abundance of the lighter nuclei (protons and helium nuclei) falls off more rapidly than the heavier nuclei with increasing energy. This indicates a trend of moving towards a heavier mass composition approaching the "knee" in the cosmic ray flux spectrum. Several other independent measurements agree with a shift toward heavier mass composition in this range - studies of high energy muons from

NOTE:
This figure is included on page 12
of the print copy of the thesis held in
the University of Adelaide Library.

Figure 1.5: *Figure taken from [164]. The cosmic ray abundances (He-Ni) measured at Earth compared to the solar system abundances, all relative to silicon: [**Solid circles**] low energy data, 70-280 MeV nucleon^{-1};[**Open circles**] Compilation of high energy measurements, 1000-2000 MeV nucleon^{-1}. [**Diamonds**] Solar system.*

cosmic ray showers [181], air shower Cherenkov light emission [67], hadronic analysis of extensive air shower cores [80] and air shower muon to electron ratios [50].

Direct mass composition measurements above 10^{15} eV are complicated by the progressively lower flux of such particles and indirect measurements via air showers is the only remaining technique. Upon entering the Earth's atmosphere, cosmic rays may collide with an atmospheric nucleus and fragment into a cascade of subatomic particles called an extensive air shower (see section 1.6). These air showers generate fluorescence and Cherenkov light through interactions with atmospheric gas and grow to a substantially sized 'footprint' upon reaching the Earth's surface - making their detection easier than trying to intercept the initiating cosmic ray primary particle directly. Measurements made via fluorescence detectors [40] by the Fly's Eye group in 1993 indicated (for a mixed proton and iron nuclei composition) a 20% proton composition at 10^{17} eV moving towards a 40% composition at 10^{18} eV [40]. This trend of moving towards a lighter composition above 10^{15} eV has also been observed by other experiments - such as in the analysis of muon rich events thought to be associated with air showers initiated by heavier nuclei [112] which found an increase to a 97% proton composition at 10^{17} eV from 90% at 10^{15} eV.

One method of studying the mass composition of a sample of cosmic rays is to look at how the mean X_{max} (depth of maximum) of air showers changes with energy. The X_{max} value is the atmospheric depth at which an extensive air shower (measured by a fluorescence detector) has the most particles. Showers initiated by heavier nuclei will tend to develop higher in the atmosphere than proton initiated showers, as the heavier nuclei initiated showers are roughly equivalent to a combination of multiple lower energy ones [131]. Figure 1.6 represents some recently reported results for the mean X_{max} values (the black markers) measured for UHECR, along with the theoretical (according to several models) expectations for purely proton and iron nuclei distributions. The results suggest a mixed composition of protons and heavier nuclei, with an apparent shift to a heavier mass composition above 2x10^{18} eV as the mean X_{max} values begin to drift further away from the expectations for a purely proton composition of particles.

NOTE:
This figure is included on page 14
of the print copy of the thesis held in
the University of Adelaide Library.

Figure 1.6: *Figure taken from [5]. Atmospheric depth X_{max} of the shower maximum as a function of energy. The data points are accompanied by their statistical uncertainties and respective number of events in each bin. The energy-independent systematic uncertainty in X_{max} is less than 15 g/cm^2. The expectations for primary protons and iron nuclei are shown for three different models of hadronic interactions.*

1.5   Acceleration mechanisms

Several possible cosmic ray acceleration mechanisms are described in this section. One of the first acceleration mechanisms ever developed involved interactions between a cosmic ray particle and the magnetic fields of several ionized gas clouds in the interstellar medium. Such an acceleration model was relatively inefficient, but a popular mechanism called diffusive shock acceleration was later developed that used the shockwaves generated by supernovae to fuel cosmic ray particle acceleration. Diffusive shock acceleration can successfully describe the measured energy spectrum at low $< 10^{15}$ eV energies but struggles to account for observations of more energetic particles - though several modifications of the model have been suggested. The problem is that the magnetic field strength and size required to confine cosmic rays

for acceleration to $> 10^{18}$ eV energies is relatively hard to come by. Several alternative theories for ultra-high energy cosmic ray production have been developed thus far, but it remains unclear exactly which mechanism to favor.
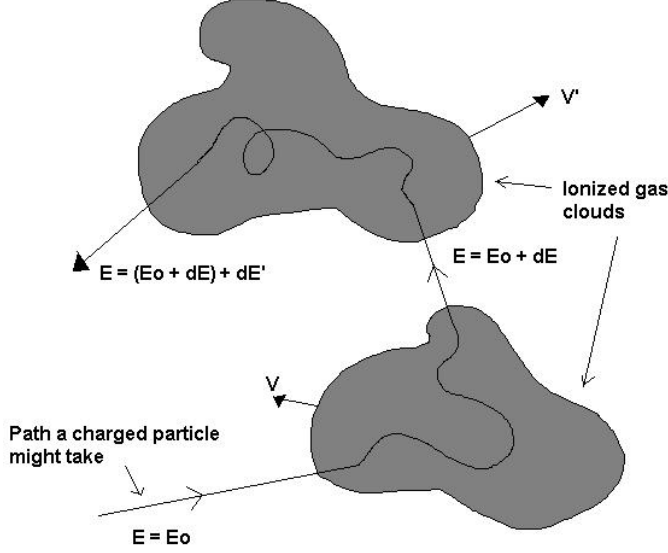

Figure 1.7: *A charged particle being accelerated through second order Fermi acceleration.*

One of the first mechanisms for cosmic ray particle acceleration was suggested by Fermi in 1949 [74]. This process is now called 2nd order Fermi acceleration and involves acceleration through interactions with randomly moving magnetic fields embedded in ionized gas clouds. This acceleration mechanism is ill-favored as the fractional increase ($\frac{\Delta E}{E}$) for each interaction is very small (since $V << c$) as seen in figure 1.7 and equation 1.4.

$$\frac{\Delta E}{E} \propto \frac{V^2}{c^2} \tag{1.4}$$

where c is the speed of light and V is the speed of the ionized gas cloud in which the magnetic field is embedded.

One of the most popular acceleration mechanisms is diffusive shock acceleration by supernova remnants or AGN (Active Galactic Nuclei) jets [32][31][36][37][41][120], from which an approximation to the experimentally measured power law type energy spectrum naturally results. Here acceleration is achieved through interactions of the cosmic ray particle with ionized gas clouds which the shockwave has both swept up and is moving towards, as demonstrated in figure 1.8. The magnetic fields of ionized gas clouds can
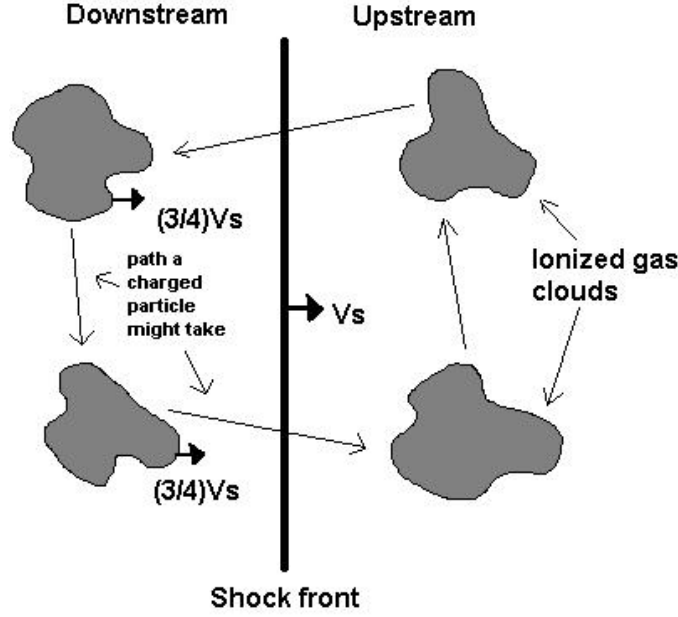
Figure 1.8: *Shows a particle moving back and forth across a shock front undergoing diffusive shock acceleration.*

deflect a cosmic ray back and forwards across the moving shock front, each time giving a fractional increase of energy proportional to the shock speed as shown in equation 1.5:

$$\frac{\Delta E}{E} \propto \frac{V_s}{c} \tag{1.5}$$

where V_s is the speed of the shock front and c is the speed of light.

In supernova shocks, the energy of cosmic rays accelerated by diffusive shock acceleration is believed to be limited to around 10^{14-15} eV due to the limited lifetime of the shocks [121], and the increasing probability of cosmic rays escaping the acceleration process as their gyroradius increases with energy. The maximum possible energy E_{max} (in units of 10^{18}eV) able to be achieved through diffusive shock acceleration is [121]:

$$E_{max} \approx \epsilon \times \beta \times Z \times B \times L \tag{1.6}$$

where β is the shock speed, $B_{\mu G}$ is the magnetic field strength (in μG) and L is the size of the acceleration region (in kiloparsecs). The efficiency ϵ, represents the efficiency of the acceleration process, and lies between 0 and 1.

Some studies suggest this limit may be lifted to higher energies if quasi-normal shocks (with magnetic fields parallel to the shock front) are

assumed [107]. Supernova shockfronts expanding directly into a stellar wind may also yield increased energies up to 10^{17} eV [176]. Diffusive shock acceleration has been experimentally observed around the heliospheric bow shock with the acceleration of charged particles originating from the solar wind [71].
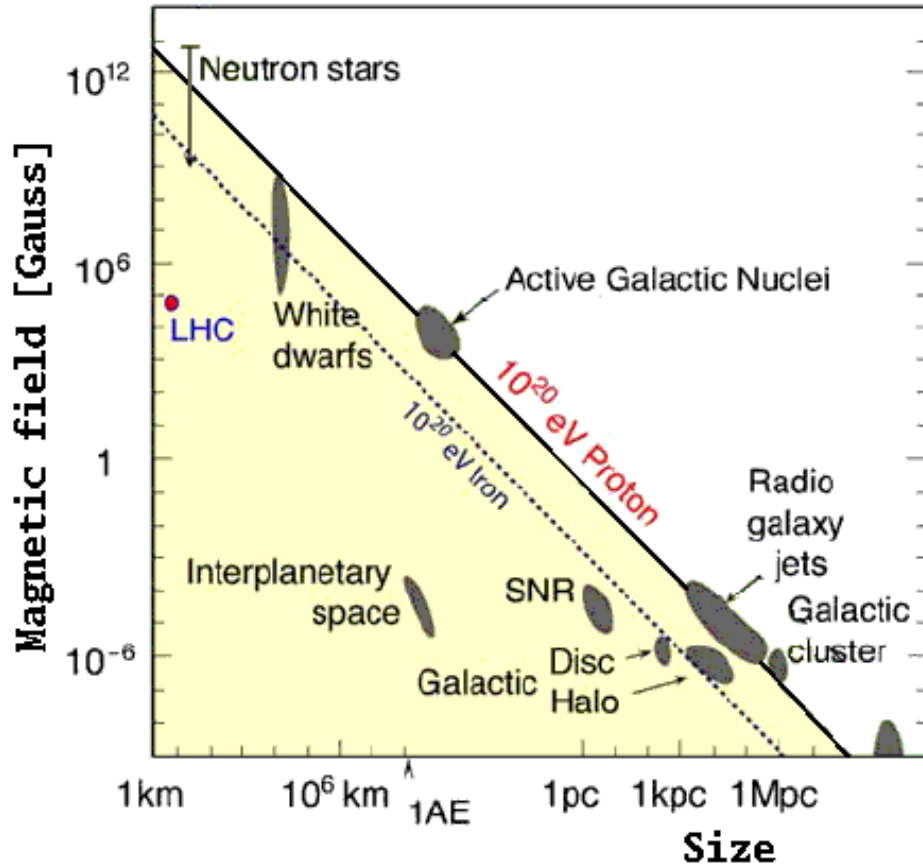

Figure 1.9: *Figure taken from [2]. A Hillas diagram. Astrophysical objects to the left of the 10^{20} eV proton and iron diagonal lines cannot accelerate particles to the energies indicated.*

Identification of acceleration sites for the $> 10^{20}$ eV UHECRs measured on Earth is a very challenging problem. Cosmic rays become successively harder to contain and accelerate with increasing energy, due to their increasing gyroradius. To achieve energies $> 10^{20}$ eV an acceleration site must be either large enough or have a strong enough magnetic field to contain it through the acceleration process. Figure 1.9 is a Hillas diagram,

representing the size and strength of the magnetic fields associated with various astrophysical objects and the minimum requirements for acceleration of 10^{20} eV cosmic ray particles. Few astrophysical objects have the magnetic field dimensions and strength to accelerate cosmic rays to these energies via shock acceleration and at this point it is still not clear which of these classes of sources are responsible - though recent measurements by the Pierre Auger Observatory have indicated a possible correlation with the Active Galactic Nuclei [10] seen in figure 1.9.

Another acceleration mechanism involves the region immediately surrounding AGN [146][173]. In this model, protons are accelerated in the black hole's accretion disk before undergoing electron capture to create neutrons. The neutrons subsequently escape the accretion disk and eventually beta decay into an antineutrino, electron and a high energy proton. These may subsequently propagate to and be detected on Earth.

Acceleration at a galactic wind termination shock may also produce high energy cosmic rays [106][108]. In this scenario, supernovae within a galaxy generate a strong enough galactic wind to create a termination shock a substantial distance away, which due to the timescale and size, may confine a cosmic ray particle long enough to be accelerated to such higher energies as 10^{20}eV. There is no observational evidence for such a galactic wind associated with the Milky Way galaxy however.

Another possible origin of cosmic rays lies in the 'top down' models. In these models, generally speaking, there is assumed to exist some super heavy 'X' particles (mass of order 10^{25}eV) that are trapped within topological defects (associated with spontaneous symmetry breaking in some Grand Unified Theories (GUTs)). These particles may be released when the topological defect decays, before subsequently decaying themselves into a combination of quarks and leptons. The quarks will subsequently hadronise - creating mostly pions, but also a small ($\approx$3%) nucleonic component [39]. Further decay of these products would mean that the bulk of the measured flux would be in neutrinos, gamma rays, electrons and positrons.

It is also possible that ultra-high energy cosmic rays may be topological defects themselves. A popular scenario is that of a magnetic monopole, after acceleration in a galactic magnetic field, initiating an extensive air shower in the Earth's atmosphere similar to a hadronic initiated one. There are practical problems however, as it is difficult for monopoles to deposit enough energy to initiate the shower, and there should be a strong observed anisotropy in arrival directions of ultra-high energy cosmic rays - which is not apparent in observations [35].

1.6 Extensive air showers

Upon entering the Earth's atmosphere a cosmic ray particle will collide with an atmospheric nucleus, initiating a cascade of subatomic particles called an extensive air shower (EAS). The subatomic particles produced in this shower may be divided into three categories - the hadronic component, the muonic component and the electromagnetic component. Neutrinos are also produced in EAS cascades but their extremely small interaction cross-sections mean they rarely play a further role in the air shower.

The hadronic component of the shower consists of the remains of the cosmic ray primary particle and impacted atmospheric nuclei, and serves to fuel both the electromagnetic (photons, electrons and positrons) and muonic (charged pions, kaons and muons) components through subsequent collisions in the atmosphere. As the air shower develops, the net number of particles increases through a variety of mechanisms while the average energy per particle drops. Eventually the average energy per particle drops to an extent where rate of particle loss exceeds the rate of new particle creation and the total number of particles in the shower begins to decrease. This process is difficult to simulate accurately for the highest energy cosmic ray primaries due to the need to extrapolate interaction cross-sections, multiplicity and inelasticity of high energy hadronic interactions in the atmosphere.

Measurement of EAS parameters allow studies of the characteristics of initiating cosmic ray particles to be made, such as their composition and energy. Extensive air showers may be detected with several techniques, such as measuring their muon density at ground level, or capturing and measuring fluorescence or Cherenkov light created by the shower. Due to the low cosmic ray flux, extensive air showers are currently the only practical way to study cosmic rays above 10^{15} eV.

Extensive air showers may also be initiated by high energy photons. Unlike hadronic primary initiated showers however, photon initiated showers will not have a hadronic component continually feeding photons (via π° decay) to the air shower. Photon induced showers will tend to develop more slowly and across greater atmospheric depths, than a proton induced shower of equivalent energy. This is because in a photon induced shower a larger number of interactions are required to lower the energy to the point where the extensive air shower casacade stops. At higher energies, photon induced showers will develop even deeper in the atmosphere due to the LPM effect [122][134] suppressing pair-production and bremsstrahlung interaction cross-sections.

1.6.1   Hadronic component

The hadronic component of an extensive air shower consists of the remnants of the initial cosmic ray particle and any impacted atmospheric nuclei. An extensive air shower begins when the cosmic ray particle first collides with an atmospheric nucleus. This collision fuels the creation of pions and kaons which contribute to the electromagnetic and muonic components of the shower, but imparts very little traverse (to its original pointing direction) momentum to the hadronic component. Subsequent collisions with atmospheric molecules continue to create high energy subatomic particles to fuel the other components of the shower.

During a collision, the cosmic ray particle passes through the nucleus of the atmospheric molecule, losing approximately half of its energy as it does so. Very little of this energy is imparted to the atmospheric nucleus - most of it being use to fuel the creation of a combination of leptons and mesons. The fraction of energy lost by the cosmic ray in the collision is termed the 'inelasticity', and the number of particles created is termed the 'multiplicity' of the interaction. Higher multiplicity implies the creation of more particles of a lower energy during an inelastic collision, while a lower multiplicity results in less particles being created, but of a higher energy. Neither the inelasticity nor multiplicity of interactions have been experimentally measured at energies associated with the highest energy cosmic rays - as none of the current particle accelerators are capable of acceleration to sufficient energies and measurements close to the fragmentation region of fixed target particle collider experiments are difficult to make.

The remains of the primary cosmic ray particle and one or two nucleons from the impacted atmospheric nucleus continue to travel with the original trajectory of the original cosmic ray particle and are known as the hadronic component of the shower. Tranverse momentum of any produced particles is very small, thus the hadronic portion of an extensive air shower is concentrated around the central axis of the shower and has spread relatively little laterally by the time the shower reaches the Earth's surface. Subsequent collisions with other atmospheric nuclei will occur - each time contributing to both the electromagnetic and muonic compononents of the shower. Overall less than 1% of the particles in an extensive air shower constitute the hadronic component.

Both the atmospheric depth at which the cosmic ray particle first interacts with the atmosphere and the frequency of subsequent collisions depends upon the cosmic ray particle's interaction cross-section, which is both energy and composition dependent. Predictions of the interaction cross-section are mainly based upon extrapolations of lower energy measurements
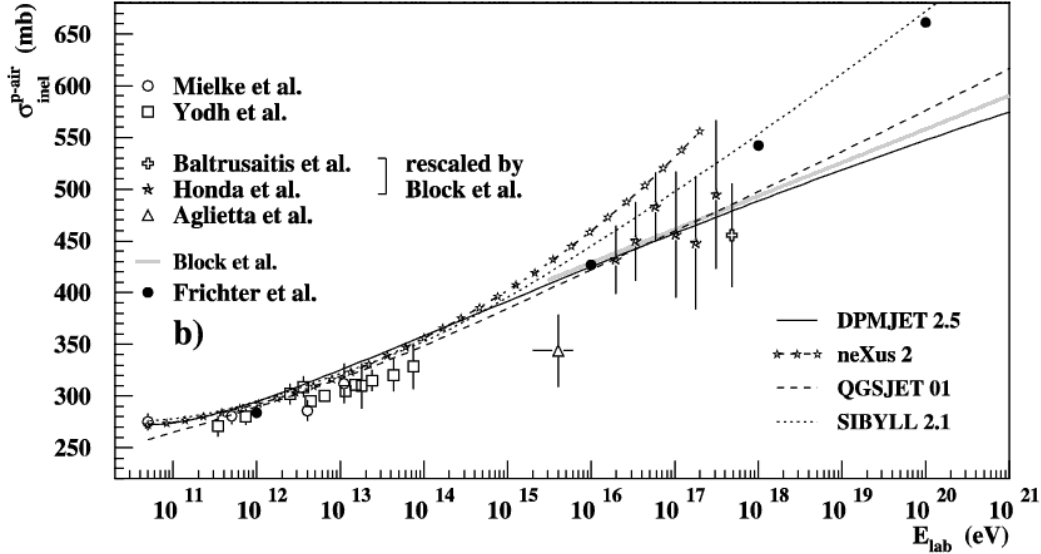
Figure 1.10: *Figure taken from [114]. Inelastic proton-air cross-sections from measurements and models. Experimental data taken from [16][33][102][133][180]. Theoretical models from [42][81].*

as demonstrated for protons in figure 1.10.

Extracting cross-section measurements directly from extensive air showers is not possible. The higher energy measurements in figure 1.10 were performed by selecting a sample of proton-induced showers (very deeply penetrating showers) and measuring the logarithmic slope of the tail of their X_{max} distribution. This slope Λ is related to the interaction cross-section σ_{inel}^{p-air} by equation 1.7 [114]:

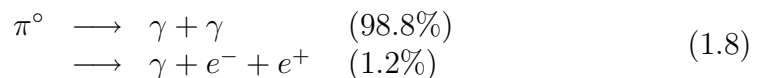$$\Lambda = 14.6 \frac{k.m_p}{\sigma_{inel}^{p-air}} \tag{1.7}$$

where m_p is the mass of the proton and k depends upon the inelasticity of the collision.

Different values of k and so hence inelasticity are assumed in different measurements, which may be brought in line with each other and the models by individually adjusting the assumed value of k [42]. A high level of inelasticity results in a fast dissipation of energy in the shower, resulting in a shower reaching its maximum number of particles higher in the atmosphere than a lower level of inelasticity.

1.6.2   Electromagnetic component

The electromagnetic component of an air shower is made up from the contributions of several mechanisms and constitutes around 90% of a shower. Photons are initially created in an extensive air shower and are the result of the decay of neutral pions created during inelastic collisions of the hadronic shower component. Other processes, such as fluorescence, Cherenkov light and bremsstrahlung also contribute later. A very important process within the electromagnetic component is pair production, whereby energetic photons create electron/positron pairs that may subsequently undergo bremsstrahlung or lose their energy through ionization processes. Eventually the average energy of shower particles becomes so low that pair production and bremsstrahlung interactions within the shower stop. The number of particles at a particular stage of a hadronic shower is difficult to calculate, but may be well described through a fitted Gaisser-Hillas function. Lateral movement (away from the shower axis) of charged particles in the electromagnetic component is a result of Coulomb scattering, and may be approximated by the NKG lateral distribution function.

Neutral pion decay is the foremost contributor of photons in an extensive air shower. Approximately a third of the energy goes into the production of neutral pions during each inelastic collison of the cosmic ray primary particle. Neutral pions have a rest mass of $\sim$135 MeV and a half life of $\sim$8x10^{-17} seconds. Photons are produced as a result of their subsequent decay via photoproduction as seen in equation 1.8.

$$
\begin{aligned}
\pi^{\circ} \quad &\longrightarrow \quad \gamma + \gamma &\quad (98.8\%) \\
&\longrightarrow \quad \gamma + e^{-} + e^{+} &\quad (1.2\%)
\end{aligned}
\tag{1.8}
$$

A source of low energy photons may be found in fluorescence and Cherenkov light produced by the shower. Atmospheric molecules such as N_2 are influenced by the passage of the shower, exciting the electrons within them to more energetic states. These electrons subsequently decay back to a less energetic state releasing a fluorescence photon [174] with energy equivalent to the difference in energy states. Cherenkov radiation is produced by charged particles within the shower that are moving faster than the local speed of light within the atmosphere. The electromagnetic fields of the shower's charged particles displace electrons and polarize atoms, which emit photons as they return to equilibrium. These photons constructively interfere with each other when the charged particles are moving faster than the speed of light in the atmosphere - forming Cherenkov radiation.

Photons with energy above 1.022 MeV (twice the rest mass of an electron) may undergoe pair production in the presence of an atmospheric

nucleus to produce an electron-position pair as seen in equation 1.9.

$$\gamma \longrightarrow e^+ + e^- \tag{1.9}$$

Lower energy photons may also undergo other processes - such as Compton scattering (< 20 MeV) with electrons and the photoelectric effect [155]. The number of photons, electrons and positrons will increase as the extensive air shower develops, but their average energy decreases.

Electrons and positrons created via the pair production process go on to create further photons via bremsstrahlung radiation. Bremsstrahlung radiation [96] is produced when charged particles are deflected by the electric fields of atmospheric nuclei. This deflection decelerates the charged particle, converting some of the charged particle's energy into a photon that contributes to the electromagnetic component. The rate of energy loss $\frac{dE}{dx}$ via this process is approximated by equation 1.10:

$$\frac{dE}{dx} = -\frac{E}{2X_0} \tag{1.10}$$

where E is the charged particle's energy and X_0 depends on the medium being traversed ($X_0 = 37.2$ g/cm^2 in air).

Photons produced via bremsstrahlung may in turn undergo pair production - creating more charged particles, and hence further photons. The interaction length for bremsstrahlung is approximately the same as that for pair production, therefore for each interval of $X_0\ln(2)$ travelled, the average energy per particle is halved and the number of particles doubled.

As the shower develops, the rate of energy lost by electrons/positrons through ionization with atmospheric molecules will increase (as the average energy per particle drops) to a point where it equals the energy going to bremsstrahlung - around positron and electron energies of 81 MeV [155]. This point of an electromagnetic shower's development is termed its 'depth of maximum' or X_{max} - being the point of the shower where it has the largest number of charged particles.

The measured X_{max} of an EAS (extensive air shower) may provide clues as to the type of particle that initiated the shower. Showers which were initiated with a lighter primary particle will have a deeper X_{max} than one initiated by a heavier primary particle. This may be explained through the superposition principle [131], whereby an air shower initiated by a particle of energy 'E' with 'A' nucleons is approximately equivalent to a combination of 'A' showers with energy $\frac{E}{A}$. As lower energy showers (and hence heavier particle induced showers) are quicker to reach the 81 MeV threshold then they will have a shallower X_{max}.

Electromagnetic cascades initiated by a photon are well understood [155], and are generally investigated by solving the coupled cascade equations 1.11 and 1.12 [156][48].

$$
\begin{aligned}
\frac{\partial \pi(E,t)}{\partial t} &= -\frac{\pi(E,t)}{\lambda_\pi(E)} + \int_E^\infty \pi(E',t)\varphi_{\pi\pi}(E',E).dE' \\
&+ \int_E^\infty \gamma(E',t)\varphi_{\gamma\pi}(E',E).dE' + \frac{\partial[\pi(E,t)\epsilon(E)]}{\partial E}
\end{aligned}
\tag{1.11}
$$

$$
\begin{aligned}
\frac{\partial \gamma(E,t)}{\partial t} &= -\frac{\gamma(E,t)}{\lambda_\gamma(E)} + \int_E^\infty \pi(E',t)\varphi_{\pi\gamma}(E',E).dE' \\
&+ \int_E^\infty \gamma(E',t)\varphi_{\gamma\gamma}(E',E).dE'
\end{aligned}
\tag{1.12}
$$

$\pi(E,t)$ number of $e^\pm$ with energy E at depth t

$\gamma(E,t)$ number of photons with energy E at depth t

$\lambda_\pi(E)$ mean free path of $e^\pm$

$\lambda_\gamma(E)$ mean free path of γ

$\varphi_{ij}(E,E').dE$ probability per radiation length that particle i of energy E produces particle j with energy between E' and $E' + dE'$

$\epsilon(E)$ rate of continuous energy loss per radiation length

Equations 1.11 and 1.12 may be solved analytically through the use of approximations. One such approximation assumes that the mean free paths for bremsstrahlung (λ_π) and pair production (λ_γ) are equal, and that energy loss by ionization (ϵ) is a constant 2 MeV/(g.cm^{-2}) in air. This yields an approximation for the total number of electrons at a depth X in a cascade initiated by a single photon of energy E_0 [83] seen in equation 1.13.

$$
N(E_0,t) \sim \frac{0.31}{\sqrt{t_{max}}} exp\left[t\left(1 - \frac{3}{2}ln(s)\right)\right]
\tag{1.13}
$$

$$
\begin{aligned}
t &= X/x_0 \text{ depth in units of radiation length } (x_0) \\
t_{max} &= ln(E_0/80 \text{ MeV}) \\
s &= 3t/(t + 2t_{max}) \text{ (the shower age)}
\end{aligned}
$$

It is not currently possible to analytically predict the development of an extensive air shower initiated by a hadronic primary particle. The Gaisser-Hillas function [82] however, has been shown to be effective in fitting both measured and simulated air shower development. This function $N(x)$ takes the form of equation 1.14:

$$
N(x) = N_{max}\left(\frac{x}{w}\right)^w e^{w-x}
\tag{1.14}
$$

$$
\begin{aligned}
x &= (X - X_0)/\lambda \\
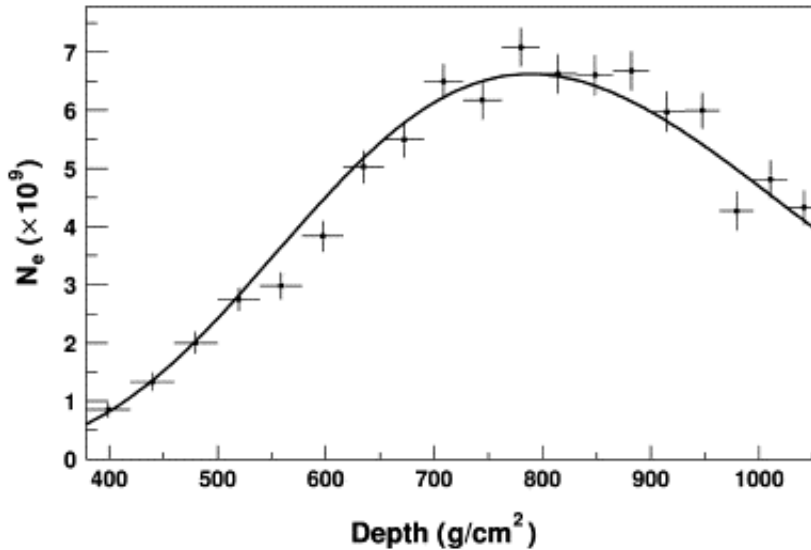w &= (X_{max} - X_0)/\lambda
\end{aligned}
$$

Figure 1.11: *Taken from [3]. Plot showing an example of a measured longitudinal profile of the number of charged particles in the shower vs atmospheric depth, and its fitted Gaisser-Hillas function. Data points with error bars are measurements made using a fluorescence detector, and the solid line is the shape of the fitted function.*

where X_0, λ, N_{max} and X_{max} are fitted parameters. X is the depth in the atmosphere measured in units of g/cm^2, and $N(x)$ is the number of charged particles in the shower.

For an extensive air shower, the development of that shower may be described as the variation of the number of charged particles with atmospheric depth. In this context, N_{max} is the maximum number of charged particles present during a shower occuring at an atmospheric depth of X_{max}. The parameter λ is usually fixed to some value (such as 70 g/cm^2) and a three parameter fit performed using N_{max}, X_{max} and X_0 [169]. The fitted X_0 parameter often takes negative values both in simulated and measured showers, so it should not be interpreted as representing the depth of first interaction of the shower. An example of a Gaisser-Hillas function fitted to a measured longitudinal profile is see in figure 1.11.

The lateral spread of the electromagnetic component is primarily the result of Coulomb scattering. After multiple Coulombic scatterings in air, a charged particle of energy E ($E >> mc^2$) experiences an average change in pointing direction $\delta\theta$ per radiation length expressed by equation

1.15 [155][62].

$$\delta\theta^2 = (\frac{21.2 \text{ MeV}}{E})^2 \tag{1.15}$$

Thus the amount of scattering suffered in the shower is inversely proportional to the energy of those electrons. Hence, electrons measured further from the central core of the shower are going to be less energetic than ones closer in, and the shower front will appear to be curved slightly (lagging around the edges) while travelling down towards the Earth.

For the electromagnetic component of an extensive air shower, the lateral density distribution $p(r)$ of charged particles may be approximated by the NKG function [109][88] (equation 1.16).

$$p(r) = \frac{N_s}{R_M^2} \frac{r^{s-2}(1+r)^{s-4.5}}{2\pi B(s, 4.5 - 2s)} \tag{1.16}$$

$$\text{where} \quad B(x, y) \quad = \quad \frac{\Gamma(x)\Gamma(y)}{\Gamma(x+y)}$$

Here $p(r)$ is the density of a total of N_s charged particles at a distance r from the shower axis, r is measured in Moliere units [142], s is the shower age and $B(x, y)$ is the standard beta function. R_m is the Moliere unit which is temperature and pressure (and thus depth) dependent. At ground level, the Moliere unit takes a value of approximately 80m.

The lateral and longitudinal distribution of the electromagnetic component of a simulated 10^{17}eV proton shower is illustrated in figure 1.12. In the left-most plot the total number/type of particles as a function of atmospheric depth is shown. In the right-most plot is shown the distribution of charged particles as a function of distance from the shower core at ground level.

NOTE:
This figure is included on page 27
of the print copy of the thesis held in
the University of Adelaide Library.

Figure 1.12: *Plot taken from [166]. Electromagnetic (·) and muon (+) components of extensive air showers initiated by 10^{17} eV protons at a zenith angle of $30°$, as simulated by the AIRES code with QGSJet hadronic model. [**Left**] Longitudinal profile (electrons scaled down by a factor of 50) [**Right**] Lateral distribution, all charged particles (X) also shown.*

1.6.3   Muonic component

The muonic component of a shower consists of muons, and the kaons and charged pions that may create them. Muons are relatively unreactive charged particles produced by several processes during the development of the shower. The foremost of these processes is the decay of low energy charged pions, whereby a combination of muons and neutrinos are produced. Another major contributor may be found through the decay of both the charged and neutral kaons produced by the hadronic component during inelastic collisions with atmospheric nuclei. Despite their laboratory half life of about 2μs, due to relativistic effects, muons produced in the shower usually reach the Earth's surface before decaying, thus the longitudinal development of the muonic component is not subject to large fluctuations. The lateral distribution of muons is also relatively flat, outnumbering particles from the electromagnetic component at greater radial distances from the shower axis.

Muons are charged particles with a very small interaction cross-section. They have a mass of $\sim$106 MeV and a mean lifetime of $\sim$2.2x10^{-6} seconds [45], before decaying into neutrinos, anti-neutrinos, positrons and electrons as seen in equation 1.17.

$$
\begin{aligned}
\mu^+ &\longrightarrow e^+ + \nu_e + \bar{\nu}_\mu \\
\mu^- &\longrightarrow e^- + \bar{\nu}_e + \nu_\mu
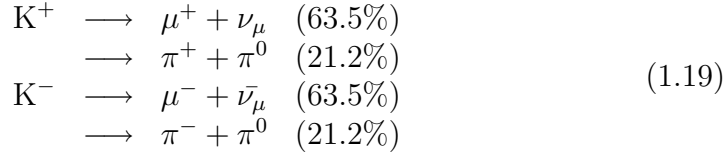\end{aligned}
\tag{1.17}
$$
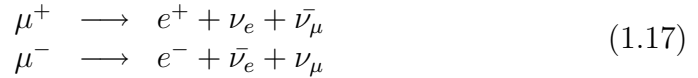
The neutrinos produced have an extremely small interaction cross-section, and so rarely contribute any further to shower development.

The primary production mechanism for muons within an extensive air shower is through the decay of charged pions produced during inelastic collisions of the shower's hadronic component. Charged pions have a mass of $\sim$140 MeV and a half-life of around 2.60x10^{-8} seconds before decaying (99.99% of the time) into muons, neutrinos and anti-neutrinos as seen in equation 1.18.

$$
\begin{aligned}
\pi^+ &\longrightarrow \mu^+ + \nu_\mu \\
\pi^- &\longrightarrow \mu^- + \bar{\nu}_\mu
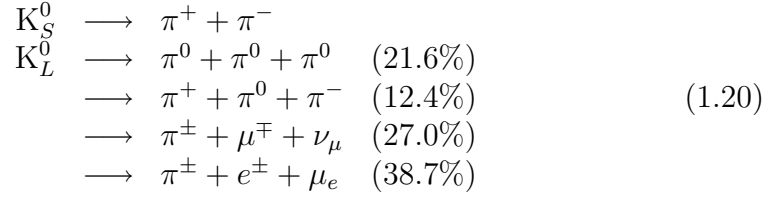\end{aligned}
\tag{1.18}
$$

Due to their relatively large lifetimes, charged pions may interact with atmospheric nuclei before decaying. Thus copious muon production does not occur until the energy of the charged pions produced is low enough such that decay is more likely than an interaction with an atmospheric nucleus. This takes place after relatively few collisions of the hadronic component with atmospheric gas. As the number and energy of charged pions depends upon the inelasticity and multiplicity of particles created during collisions of the hadronic component, the total number of muons produced during the shower is related to these three parameters.

Another production pathway for the shower's production of muons is through the decay of kaons. Approximately 10% of the particles produced during inelastic collisions are kaons, which have a mass of 494 MeV and a decay half life of 1.2×10^{-8} seconds. These kaons take the form of both the charged (K^+ and K^-) and neutral varieties ($\bar{K}^0$ and K^0). Charged kaons produced may subsequently decay into charged pions or muons as seen in equation 1.19.

$$
\begin{aligned}
K^+ &\longrightarrow \mu^+ + \nu_\mu \quad (63.5\%) \\
&\longrightarrow \pi^+ + \pi^0 \quad (21.2\%) \\
K^- &\longrightarrow \mu^- + \bar{\nu}_\mu \quad (63.5\%) \\
&\longrightarrow \pi^- + \pi^0 \quad (21.2\%)
\end{aligned}
\tag{1.19}
$$

Neutral kaons occur in quantum mechanical mixed states K_S^0 (with a mean lifetime of 8.96×10^{-11} seconds) and K_L^0 (with a mean lifetime of 5.18×10^{-8} seconds) and have a variety of decay modes seen in equation 1.20, which will subsequently contribute to the muon or electromagnetic components of the shower.

$$
\begin{aligned}
K_S^0 &\longrightarrow \pi^+ + \pi^- \\
K_L^0 &\longrightarrow \pi^0 + \pi^0 + \pi^0 \quad (21.6\%) \\
&\longrightarrow \pi^+ + \pi^0 + \pi^- \quad (12.4\%) \\
&\longrightarrow \pi^\pm + \mu^\mp + \nu_\mu \quad (27.0\%) \\
&\longrightarrow \pi^\pm + e^\pm + \mu_e \quad (38.7\%)
\end{aligned}
\tag{1.20}
$$

Muons may also be produced through γ-ray pair production and via photo-production of pions, but these processes are only significant for showers with a cosmic ray primary energy of $>10^{18}$ eV [132].

Muons have a long attenuation length and lose energy primarily through ionization at a rate of $\sim$2 MeV g/cm^2. Some small energy loss via bremsstrahlung also occurs. Recent simulations [54] show a mean free path for bremsstrahlung of around 10^5 g/cm^2 for a muon of energy 1 GeV, which for the Earth's atmosphere spanning only $\sim$1000 g/cm^2, is negligible. Pair production interactions (for muons) have a similar mean free path at energies of 1 GeV, which decreases with energy - only becoming a strong energy loss process for high energy showers at large zenith angles. The slow rate of attenuation also means that at ground level, the muonic shower component contains 5-6 times the energy contained in the electromagnetic component [88]. For low energy extensive air showers (10^{11}-10^{14} eV) only the muonic component is detectable at ground level.

The muon count of an extensive air shower is sometimes used to estimate the energy of that shower. One of the two problems associated with this approach is that if a shower of a particular energy happens to develop more deeply in the atmosphere then usual, then the muon count will be low

at ground level, and the energy will be underestimated.

The mass composition of the initiating primary particle affects the number of muons produced - with heavier nuclei producing more muons than a proton at a particular energy. The number of muons expected to be observed for a shower of given energy E can be seen in equation 1.21, where A is the mass number of the primary particle, and B and C are model-dependent constraints [27].

$$N_\mu = AB \left(\frac{E}{A}\right)^C \tag{1.21}$$

Thus a heavy iron nuclei induced air shower will produce more muons than a proton induced shower of equal energy, as N_μ is proportional to the mass number of the primary particle (as C is usually around 0.85).

The lateral distribution $\rho(N,r,k)$ of muons may be described by equation 1.22 [89], where N is the total number of muons, r is the radial distance, and k is a function depending upon shower age and zenith angle [93].

$$\rho(N,r,k) \propto \left(\frac{N}{r}\right)^{0.75} \left[1 + \left(\frac{r}{k}\right)\right]^{-2.5} \tag{1.22}$$

Muons are not significantly affected by Coulomb scattering, unlike air shower electrons, and their initial tranverse momentum is very small, deriving from what their kaon and pion parent particles originally had. An example for the lateral distribution of muons within a 10^17 eV proton shower may be seen in figure 1.12.

Chapter 2

The Pierre Auger Observatory

The Pierre Auger Observatory is the result of a collaboration of over 50 institutions and 400 individuals from around the world. The observatory studies ultra-high energy cosmic rays through the extensive air showers they initiate in the Earth's atmosphere. Both water-Cherenkov surface detectors and atmospheric fluorescence detectors are employed by the observatory, measuring extensive air showers in two independent ways. Measurements from both types of instruments may be combined to provide a superior analysis of extensive air showers. Currently two independent observatories are planned, one in the Northern hemisphere in the state of Colorado, and another in the Southern hemisphere in the Mendoza province of Argentina. The Southern observatory is complete, while the Northern one is still in the planning stages.

2.1   Surface detectors

The Southern Pierre Auger Observatory studies extensive air showers initiated by cosmic rays through four fluorescence detectors spaced around a vast array of surface water-Cherenkov detectors. Over 1600 of these water-Cherenkov detectors have been installed at the observatory, spaced 1.5 km apart and covering an area of over 3000 km^2. Water-Cherenkov detectors record air showers through the Cherenkov light produced by charged particles (created by the shower) as they pass through the detector. These measurements allow a determination of the geometry of the initiating cosmic ray to be made, along with providing information on their original energy and mass composition.

2.1.1   Operation

Each water-Cherenkov surface detector essentially consists of a tank containing 12 tonnes of pure water with three photo-multiplier tubes. Each tank is ~1.55 m high with a diameter of ~3.6 m, lined with reflective Tyvek and filled with water to a depth of 1.2 m. Three 9" photomultiplier tubes are positioned above and face down into the water. Data recorded by the photomultiplier tubes is transmitted via a wireless local area network communications antenna to control facilities located at each of the Auger fluorescence detectors, before being forwarded via a microwave link for analysis. Each surface detector operates automously, being powered by a solar panel and battery. A single Auger surface detector may be seen in figure 2.1.

NOTE:
This figure is included on page 32
of the print copy of the thesis held in
the University of Adelaide Library.

Figure 2.1: *Image adapted from [28]. An image of one of Auger's surface water-Cherenkov detectors with major compnents labelled.*

As muons from extensive air showers pass through an Auger water-Cherenkov detector they emit Cherenkov radiation which is then scattered by the water and tank Tyvek lining before being recorded by the detector's photomultiplier tubes (PMTs). There is an approximately uniform response

by the PMTs for vertically downward travelling muons incident at different points of the tank, as seen in the top plot within figure 2.2. If the PMTs were to be located at the bottom of the water detection volume then the response would no longer be uniform, as seen in the lower plot of figure 2.2 where the three spikes represent regions where extra signal will be measured from incident muons. This is due to Cherenkov radiation (which is directed in a cone-like shape along the axis of movement of its parent muon) directly illuminating the PMTs. Incident particles with large zenith angles ($> 48°$) may still produce Cherenkov radiation that directly illuminates PMTs mounted on the roof of the detector.

Subtle differences between tanks and the gain of their photomultiplier tubes means that each individual water-Cherenkov detector must be calibrated. One of the most important calibrations is to ensure each of a detector's PMTs are gain matched. This is achieved for each PMT individually by adjusting gain until a trigger rate of approximately 100 Hz above a threshold of 2.8 times the desired value for a VEM[1] (50 ADC counts) is observed [179]. This is the expected trigger rate (measured independently using a test detector [179]) resulting from atmospheric muons and it provides a common point of reference for calibrating the PMTs within a detector.

A local system controller continously measures the signal being measured by the detectors PMTs. There are two kinds of triggers handled by this local software - T1 and T2 triggers. T1 triggers may be tripped at a rate of approximately 110 Hz and may be the result of a three-fold signal coincidence above 1.75 VEM, or a time over threshold (ToT) trigger. This trigger results in data recently recorded by the station being stored locally ready for further use if necessary. The T2 trigger is tripped at a rate of around 20 Hz, and occurs when a time over threshold condition is satisfied.

Whenever a station trips the T2 trigger that station's ID, timestamp and type of trigger are fowarded to CDAS (central data acquisition system). For a given T2 triggered station, other stations also triggered within 25 μs of that trigger are examined for spatial correlation. Spatial correlation between the stations is described in terms of 'mCn', where 'm' is the number of triggered stations within the nth ring from the station being considered (see figure 2.3). The minimum condition for identifying a cluster of triggered surface detectors is a minimum of 4 triggered stations satisfying at least a "2C1&3C2&4C4" condition. That is - 2 triggered stations within the first ring, 3 within the second ring and 4 within the fourth ring, an example of which may be seen in figure 2.3. Three tanks triggered with a ToT trigger

---

[1]1 VEM is the average amount of charge deposited by a centered and vertically travelling high energy muon travelling through an Auger surface detector.

NOTE:
This figure is included on page 34
of the print copy of the thesis held in
the University of Adelaide Library.

Figure 2.2: *Taken from [27]. Simulated non-proportionality plot for the reference design water Cherenkov detector unit. Many 1 GeV muons were injected vertically at random positions over the detector top surface, and the resulting photoelectron yields averaged in 10 cm square bins. The vertical axis scales are relative to the overall mean signal in the down looking case. The upper plot shows response with PMTs placed at the top looking down, and the lower plot is identical with the PMTs at the bottom looking up.*

NOTE:
This figure is included on page 35
of the print copy of the thesis held in
the University of Adelaide Library.

Figure 2.3: *Taken from [91]. Illustration of a minimum "2C1&3C2&4C4" condition. Triggered tanks are represented as full points. The first ring has one trigger (2C1 condition). The triggered tank in the second ring fulfills the 3C2 condition. The last tank can be as far as in the fourth ring because of the 4C4 condition.*

satisfying a "2C1&3C2" condition may also be considered to be a cluster. An additional constraint is used, demanding that each of the T2 triggered tanks are within (6+5n) μs of the central tank. If both these spatial and time constraints are passed, then the cluster of triggered stations is considered a T3 triggered event.

A T3 trigger does not necessarily mean that the cluster of T2 triggered stations are result of an extensive air shower, as chance coincidences of multiple low energy showers and single cosmic muons may trigger a T3 condition. The T4 trigger condition attempts to identify those T3 triggered events that are actually the result of extensive air showers of interest. These are T3 events satisfying at least a 4C1 condition or a 3C1 condition where the three stations have triggered via the ToT condition. The difference between the start times of the triggered stations must also be lower than the distance between them divided by the speed of light. A further T5 trigger excludes events that fall too close to the edge of the Auger array.

2.1.2 Geometry

An extensive air shower may be approximated as a planar front of particles, propagating at the speed of light along an axis ($\bar{a}$) defined by the pointing direction of the initiating primary particle, as seen in figure 2.4. The time ($\hat{t}_i$) at which the shower plane crosses some SD detector at point $\bar{X}_i$ may be

written as equation 2.1:

$$\hat{t}_i = \frac{1}{c}\left(ct_0 - (\bar{X}_i - \bar{X}_b) \bullet \bar{a}\right)$$ (2.1)

where c is the speed of light, t_0 is the surface arrival time of the shower core, and $\bar{X}_b$ is a first approximation of $\bar{X}_0$.

The predicted arrival time $\hat{t}_i$ may be fitted using a standard least squares fit, where χ^2 in equation 2.2 is calculated using all the triggered stations, and the time-variance σ_{t_i} is defined in [103]. There are three free parameters to be fitted, t_0 and two components of $\hat{a}$.

$$\chi^2 = \sum_i \left[\frac{t_i - \hat{t}_i}{\sigma_{t_i}}\right]^2$$ (2.2)
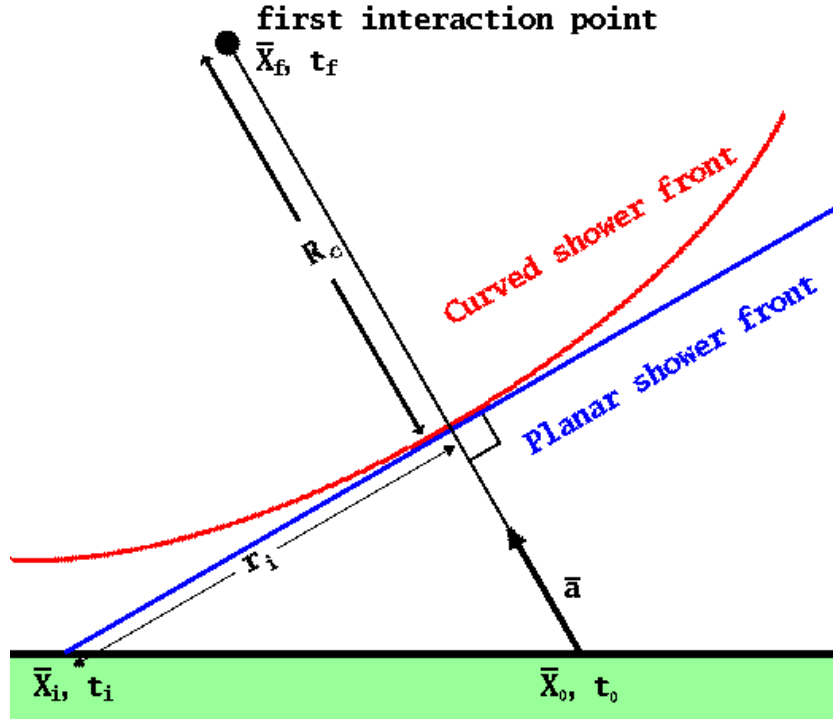
Figure 2.4: *Shows the geometry and parameters used for SD based reconstruction of an extensive air shower.*

A more realistic curved shower front may be fitted to data by adding a spherical term as seen in equation 2.3 and an additional free variable R_c

describing the radius of curvature of the shower front.

$$\hat{t}_i = \frac{1}{c}\left(ct_0 - (\bar{X}_i - \bar{X}_b)\bullet\bar{a} + \frac{r_i^2}{2R_c}\right)$$ (2.3)

$$\text{where} \quad r_i \quad = \quad |\bar{a} \text{ x } (\bar{x}_i - \bar{x}_b)|$$

The angular resolution calculated by this fit has been found to be better than
0.9° for events with more than 5 triggered surface detectors and better than
1.2° for events with only 4 or 5 triggered detectors [43][30].

While the triggering times of the surface detectors are used to determine the pointing direction of the shower, the measured signal strengths are used to estimate both the shower size and core position. The signals measured by the water-Cherenkov detectors are modelled as a function of distance from the shower core. This lateral distribution function (LDF) (seen in equation 2.4) $S(r)$ describes the measured signal in units of VEM at a surface detector a distance r from the shower core, and is a modified version of the NKG (Nishimura, Kamata, Greisen) function [88][109].

$$S(r) = S(1000)\left(\frac{r}{1000}\right)^{\beta}\left(\frac{r_s + r}{r_s + 1000}\right)^{\beta}$$ (2.4)

$S(1000)$ is the signal measured 1 km from the shower core and $r_s = 700$.
The β variable describes the slope of the LDF and depends upon the zenith angle θ of the shower as seen in equation 2.5, where a, b and f are constants described in [157].

$$\beta(\theta) = \begin{cases} a + b(sec\theta - 1) & sec\theta < 1.55 \\ a + b(sec\theta - 1) + f(sec\theta - 1.55) & sec\theta \geq 1.55 \end{cases}$$ (2.5)

$$\text{or} \quad \beta_{(\theta)} \quad \approx \quad \text{-3.69} + 1.17sec\theta$$

Equation 2.4 is fitted with measured data through a simple minimization of the χ^2 function seen in equation 2.6.

$$\chi^2 = \sum_i \left[\frac{S_i - S(r_i)}{\sigma_{S_i}}\right]^2$$ (2.6)

σ_{S_i} describes the tank signal accuracy [6], which depends upon the shower axis zenith angle. In total there are three parameters being fitted in equation 2.6 - the shower size $S(1000)$ parameter and two components from the shower core. The integral of the measured tank signal is sensitive to fluctuations in shower development, therefore the signal 1000 m from shower core ($S(1000)$)

is used to classify the size of a shower [99][100], since it is at this distance that fluctuations are expected to be minimized [138].

The ability of the LDF to describe extensive air showers is limited to "vertical" events - showers arriving at a zenith angle of less than $60°$. "Horizontal" showers (zenith angles $\geq 60°$) develop similarly to vertical ones, but due to the extra atmospheric pathlength (and so hence attenuation) only have their muonic componenent arriving at the Earth's surface. The extra traversal time means that the distribution of muons in the air shower will be significantly distorted by the geomagnetic field [29], for which the LDF function (equation 2.4) is no longer a good description.

2.1.3   Energy measurement

The $S(1000)$ parameter may be used as an estimator for the energy of an extensive air shower measured by Auger surface water-Cherenkov detectors. This parameter is measured through the fitting of the LDF to signals measured by multiple surface detectors (see section 2.1.2), and represents the signal strength expected to be measured at a lateral distance of 1000m from the shower core at ground level. At this distance, fluctuations between individual showers at the same energy and zenith angle are expected to be minimal [138].

NOTE:
This figure is included on page 38
of the print copy of the thesis held in
the University of Adelaide Library.

Figure 2.5: *Taken from [7]. [**Left**] Integrated number of events at $cos^2\theta$ for an indicated minimum value of $S(1000)$. [**Right**] $CIC(\theta)$ function describing $S(1000)$ attenuation with zenith angle, fitted with quadratic function.*

Due to differences in atmospheric attenuation, showers of identical energy will have different measured values of $S(1000)$ depending upon their zenith angle θ. The functional form of this attenuation is derived by considering the overall signal (in terms of VEMs) being measured by the surface

detectors. The left-most plot in figure 2.5 represents the integrated number
of VEMs arriving with respect to zenith angle above various event intensity
cut-offs. Note that the rate of change of flux at a particular zenith angle is
approximately constant regardless of the cut-off used.

   If a flux of muons is assumed such that the flux of 'VEMs' is identical
from all arrival directions, then the left-most plot may be used to derive a
function CIC(θ), describing the expected change in S(1000) value with zenith
angle. The CIC function is a quadratic function fitted to measured data, as
seen in the right-most plot in figure 2.5. The quadratic fit (equation 2.7)
seen in figure 2.5 was performed using an intensity cut of 128 events with
$a = 0.94 \pm 0.06$ and $b = -1.21 \pm 0.27$. The choice of a particular intensity
cut-off is not critical, as the shape of the attenuation curve changes only
slightly with different cut-offs.

$$CIC(\theta) = 1 + ax + bx^2 \tag{2.7}$$

$$\text{where} \quad x \quad = \quad \cos^2 \theta - \cos^2 38° $$

   Equation 2.7 allows an estimation of the S(1000) parameter that
would be measured for a particular shower at different zenith angles. The
average zenith angle θ of "vertical" showers ($\theta < 60°$) is 38°. Therefore
the value which S(1000) takes (S_{38}) at a zenith angle θ is estimated using
equation 2.8 and then used in shower energy estimations.

$$S_{38} = \frac{S(1000)}{CIC(\theta)} \tag{2.8}$$

Uncertainties in S_{38} therefore depend upon uncertainties in the measured
S(1000) and zenith angle parameters. Measured S(1000) uncertainties arise
as a result of uncertainty in measured signal (due to the finite size of the
surface detectors) and the lack of the knowledge of the 'true' shape of the
LDF function [8]. Uncertainties in reconstructed zenith angle depend upon
the number of stations triggered by the extensive air shower.

   The relationship between the S_{38} parameter and shower energy may
be determined using theoretical models of extensive air shower development
or experimentally measured hybrid events. A hybrid event is an extensive
air shower that has been measured by both Auger's fluorescence and surface
detectors. Surface detector information is used to constrain the geometry
of a shower while the fluorescence detector provides an almost calorimetric
measurement of the energy. As fluorescence detector based measurements are
only available on clear moonless nights, only ~15% of air showers measured
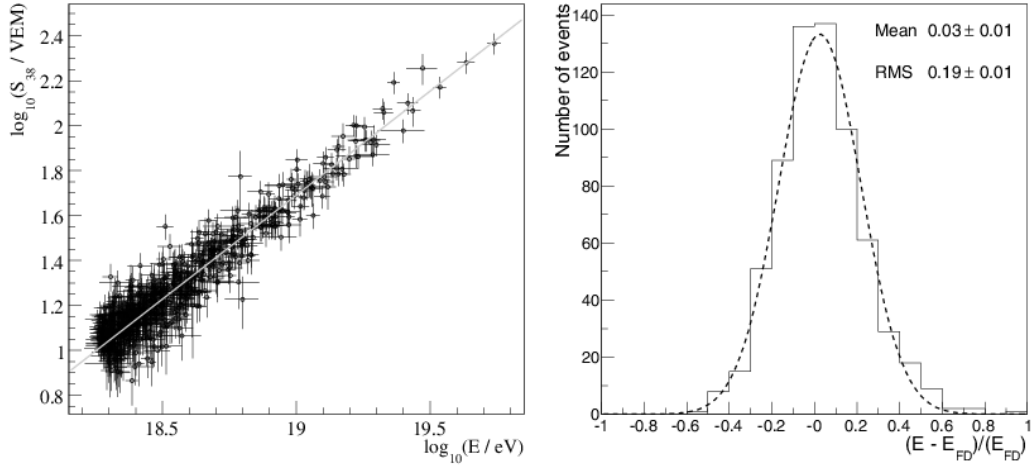at the Pierre Auger Observatory are hybrid events.

Figure 2.6: *Taken from [14]. [**Left**] Fitted relation between S_{38} parameter and shower energy measured by fluorescence detector. [**Right**] Difference between the energy assigned to surface detector measurement and that measured by a fluorescence detector.*

Figure 2.6 demonstrates the correlation between the surface detector measured S_{38} parameter and hybrid event based energy measurement. The relationship between FD measured energy E_{FD} and the S_{38} parameter may be described by equation 2.9, where a and b are the fitted parameters.

$$E_{FD} = aS_{38}^b \qquad (2.9)$$

For the fit shown in equation 2.9, $a = 17.08 \pm 0.03$ and $b = 1.13 \pm 0.02$ [7]. As seen in the right-most plot, a dispersion of 19% remains for this particular calibration and is due to the hybrid event reconstruction procedure and shower fluctuations. This relationship may be used to predict a shower energy for all SD measured events with a total systematic uncertainty of 22% [7].

2.1.4   Mass composition

Conclusions about mass composition are difficult to make on an individual shower basis due to fluctuations in shower development. One of the most promising methods for determining mass composition is therefore through the analysis of large quantities of showers at a particular energy. Due to the superposition principle the depth of maximum shower development (X_{max}) is a mass composition sensitive parameter. While the Pierre Auger Observatory's surface detector array does not explicity measured the X_{max} parameter,

it may be inferred from the measured signal rise time. Comparing the average measured X_{max} value with theoretical expectations for different mass compositions provides information about the general mass composition of the cosmic ray flux.

The superposition principle indicates that an extensive air shower initiated by a nucleus with mass A and energy E is approximately equivalent to A proton showers of energy E/A. Therefore, on average, an air shower initiated by a non-proton hadronic nucleus will generally develop over a shorter distance at a higher altitude than a shower of equal energy initiated by a proton, and thus also have a smaller X_{max} depth[2].

Showers that develop earlier with a shallower X_{max} will also have less difference in path length (between the shower axis and surface) between muons created early in the shower and those later on. Thus muons created during a cascade initiated by an energetic proton will arrive at the surface over a longer period of time than those created during a heavier hadronic cascade. Therefore there is a correlation between the arrival time of muons, the depth of a shower's maximum (X_{max}) and hence shower composition.

The arrival time of muons at a surface detector may be described through the rise time $t_{1/2}$ parameter. The rise time $t_{1/2}$ for a triggered detector is defined as the time a signal takes to increase from 10% to 50% of its total integrated signal. This is demonstrated in figure 2.7, where the time between the 10% and 50% mark of the integrated signal is found to be 81.39 ns. At a particular energy the measured rise time $t_{1/2}$ will generally be greater for a proton induced air shower, than a heavier hadronic nuclei induced one.

The correlation of rise time with X_{max} (and hence mass composition) is demonstrated in figure 2.8. Differences in recorded rise times between different zenith angle groups of showers are greater for proton showers due to greater X_{max} fluctuations. The relationship between X_{max} and $t_{1/2}$ lends itself to a model dependent parameterization that allows an estimate for the X_{max} of a shower to be made based on surface detector data. Fluctuations between individual showers make mass composition analysis on an individual shower basis unreliable. Calculating the mean X_{max} value for a particular energy range however, allows comparison with the expected X_{max} means for pure compositions (i.e. only proton or iron showers) and thus studies of the general trend of the mass composition may be made.

The $t_{1/2}$ approach is heavily model dependent, requiring Monte Carlo simulated data to calculate the $t_{1/2}/X_{max}$ parameterization. The Pierre

---

[2]The depth at which a particular extensive air shower's number of charged particles is at a maximum

NOTE:
This figure is included on page 42
of the print copy of the thesis held in
the University of Adelaide Library.

Figure 2.7: *Taken from [136]. Risetime ($t_{1/2}$) of a simulated signal.*

NOTE:
This figure is included on page 42
of the print copy of the thesis held in
the University of Adelaide Library.

Figure 2.8: *Taken from [166]. Correlation between X_{max} and rise time $t_{1/2}$ 500m from shower core, for 10^{17} eV extensive air showers simulated by COR-SIKA/SIBYLL. Populations of showers at several different zenith angles are shown. [**Left**] Proton induced showers. [**Right**] Iron nuclei induced showers.*

Auger Observatory however provides independent measurements of the X_{max} of showers in conjunction with measured rise time values via hybrid measurements with fluorescence detectors. This allows a more accurate parameterization between the two parameters, but final analysis still depends upon the expected mean X_{max} values for different compositions at different energies which are model dependent.

Any correlation between rise time and X_{max} must take account of asymmetry in the measured rise time with respect to shower azimuth angle however. Surface detectors at different radial distances from the shower core at ground level will record different rise times as particles measured on the upper side of the shower core will have travelled a greater distance than those measured 'below' the shower axis. The muonic component is relatively unaffected by the extra distance travelled, but the electromagnetic component of the shower suffers measurable attenuation resulting in a shorter measured rise time in detectors on the far side of the shower core.

This effect is demonstrated in figure 2.9. The axis of an air shower is shown to be impacting within an array of blue and red coloured surface detectors within the bottom plot. Red detectors are those 'beneath' the shower axis and are expected to have greater rise times than blue stations (with equivalent radial distance from the shower core) on the far side of the impact site. Variation of measured rise time with shower azimuth (also described in the bottom plot) is shown in the top plot for various radial distances from the shower core. The rise time parameter generally decreases with azimuth angle, with stations at greater radial distances show an enhanced effect due to the correspondingly larger difference in pre-measurement shower particle path length. A parameterization providing a corrected risetime ($t'_{1/2}$) may be created [136], taking the form of equation 2.10:

$$t'_{1/2} = t_{1/2} + \delta(\theta) r \cos(\phi) \tag{2.10}$$

where $t_{1/2}$ is the measured risetime, $\delta(\theta)$ is the correction factor, r is the radial distance and ϕ is the azimuth angle with respect to the shower axis.

The degree of azimuthal asymmetry of a set of showers may be measured through the use of the asymmetry factor 'b/a'. The variables a and b are fitted parameters for particular measured zenith angles and energies in equation 2.11:

$$< t_{1/2}/r > (\theta, E) = a + b \cos(\phi) \tag{2.11}$$

where $< t_{1/2}/r > (\theta, E)$ is the average of the risetimes divided by distance from the shower's core, and ϕ is the shower's azimuth angle.

The asymmetry factor is zenith angle dependent, as asymmetry in the measured risetimes depends upon the differences in path length trav-
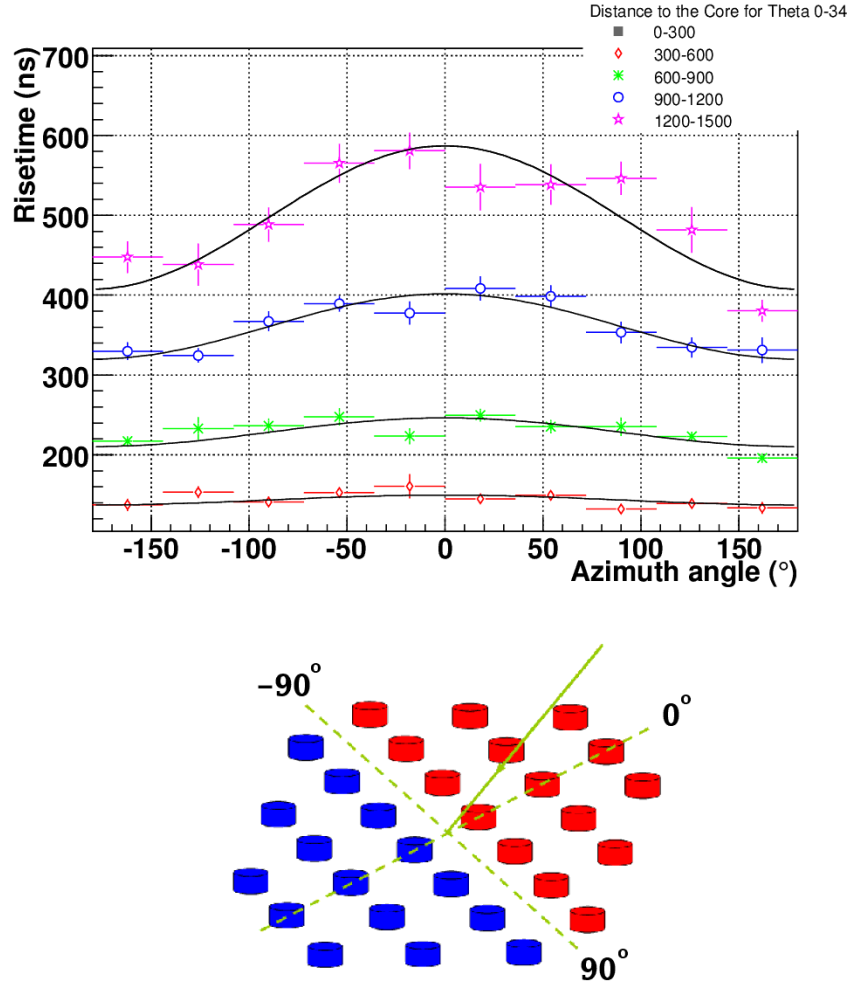
Figure 2.9: *Adapted from [136] and [84].* **[Top]** *Variation of measured rise times* ($t_{1/2}$) *with shower azimuth angle at several different radial distances from shower core.* **[Bottom]** *Diagram describing the azimuthal geometry used in the top plot.*

elled by particles in the electromagnetic component of the shower (due to their small interaction cross-section, muons do not contribute significantly to asymmetry). This dependence is demonstrated in figure 2.10, which was created by Monte Carlo simulations of iron and proton induced showers at 10^{19} eV. As seen in the figure, for small zenith angles the difference in path length between particles is minimal, resulting in little asymmetry. Increasing the zenith angle increases the asymmetry, as differences in path length increase. At very high zenith angles however, the shower's electromagnetic component becomes severely attenuated and thus despite large path differences, the sig-

nal becomes increasingly dominated by the shower's muonic component and thus less asymmetric.
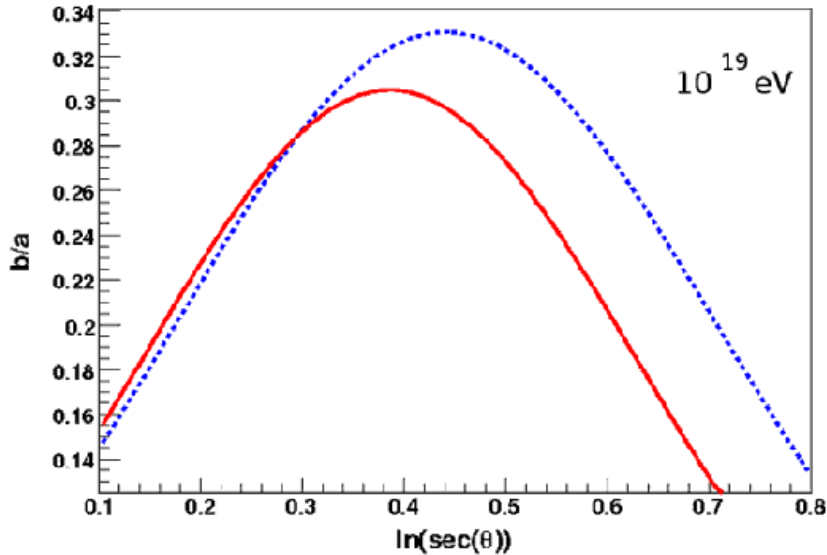

Figure 2.10: *Adapted from [69]. Monte Carlo generated 10^{19} eV showers demonstrating variation of the asymmetry parameter with zenith angle. The dashed line was generated from simulated proton induced showers, whilst the solid line was generated from iron nuclei induced showers.*

The value of $\sec(\theta)$ at which the asymmetry factor is at a maximum is called the 'XAsymMax' parameter. This parameter has a strong correlation with the average X_{max} value measured at a particular energy [69]. Using either Monte Carlo models or hybrid Auger data to calibrate, it is possible to estimate the mean X_{max} value for a set of showers measured by the Auger surface detectors, and thus may be used as a measure of mass composition [21].

2.2 Fluorescence detectors

There are four fluorescence detectors installed at the Southern Pierre Auger Observatory, each located at the edge and overlooking the surface detector array. Each fluorescence detector consists of six individual fluorescence telescopes that operate during dark moonless nights (∼15% of the time). These telescopes measure the emitted fluorescence light from nitrogen molecules excited by the passage of extensive air showers. The quantity and direction

of this measured light allows the initiating cosmic ray's geometry, energy and mass composition to be studied.

2.2.1   Operation

A fluorescence telescope's field-of-view covers a swath of sky, ranging from $2°$ to $30.6°$ in elevation and $30°$ in azimuth. Therefore with its six telescopes, each Auger fluorescence detector covers a full $180°$ of azimuth angle. As seen in figure 2.11, each individual fluorescence telescope consists of an aperture system and a spherical mirror focussing light upon an array of 440 photomultiplier tubes.

NOTE:
This figure is included on page 46
of the print copy of the thesis held in
the University of Adelaide Library.

Figure 2.11: *An overview of a fluorescence telescope.*

The aperture of an Auger fluorescence telescope consists of a diaphragm, a corrector ring and a UV transmitting filter. The filter takes the form of 3.25 mm thick, 80 x 40 cm^2 sheets of M-UG6 glass. This glass transmits nitrogen fluorescence in the near-UV, but blocks most of the other light

generated by a night sky which would otherwise increase the background noise measured by the photomultiplier tubes. The theoretical signal to noise ratio improvement in measurement due to the filter is a factor of 2 [1]. Transmission of light peaks at around 80% at 350 nm and drops to 20% at 300 and 400 nm.

The effective aperture area of the telescope is increased through the use of an annular corrector ring [160][149], seen in figure 2.12. Annular corrector rings are constructed from 24 individual plates of UV transmitting glass, each with an appropriate profile to compensate for spherical aberration. These plates extend 25 cm into the circular aperture and double the effective aperture of the telescope.
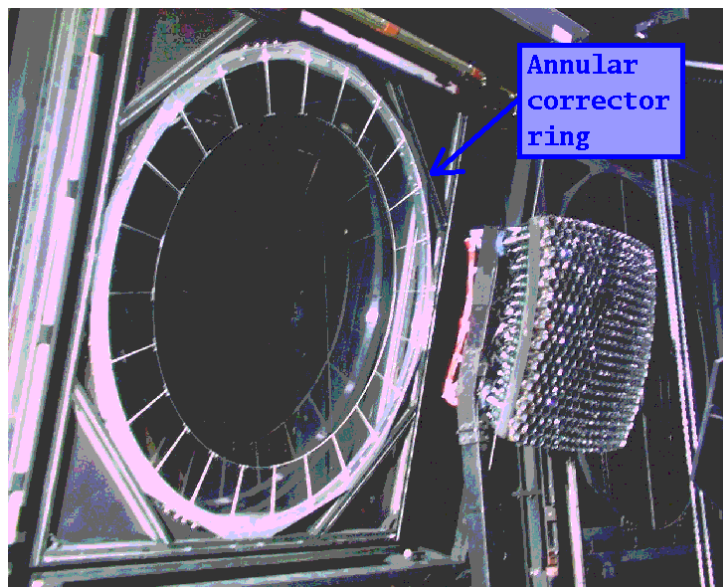

Figure 2.12: *Picture of an annular corrector ring placed around the telescope aperture.*

Transmitted UV light from the aperture is reflected by a spherical mirror onto an array of photomultiplier tubes. The mirror is formed from 36 individual fragments, aligned on and with a precise adjustable mechanical support. Mirror segments have a radius of curavature of 3.4 m and a reflectivity of around 90% between 300-400 nm. The focal plane is spherical and concentric with the mirror, with a radius of curvature of 1.743 m.

The camera portion of the telescope consists of an array of 440 photomultiplier tubes. On average each photomultiplier tube (see figure 2.13) has a 93% light collection efficiency in the 300-400 nm band [73]. These tubes,

equipped with light collectors, are placed with equal angular separation over the mirror's focal plane, but due to the curvature of the mirror have a slight difference in effective collection area [19]. Tubes are individually equivalent to a hexagonal shaped pixel with approximately 1.5° field of view and are arranged in a 20 column by 22 row format, giving each telescope a total 28.6° by 30° azimuth field of view.

NOTE:
This figure is included on page 48
of the print copy of the thesis held in
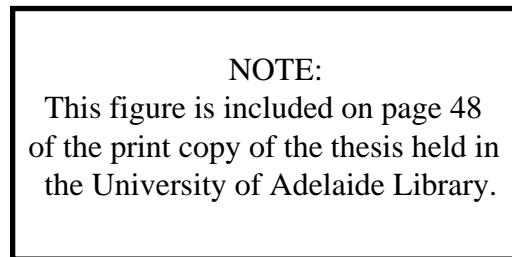the University of Adelaide Library.

Figure 2.13: *Picture of a photomultiplier tube used in the Pierre Auger Observatory's fluorescence detectors.*

Fluorescence detector pixels are calibrated through the use of a 'drum illuminator' [44] placed over a particular telescope's aperture. This drum is 2.5 m in diameter and provides a light source and uniform illumination for all the pixels that make up a particular telescope. The drum illuminator contains a single LED, emitting light in single band around 375 nm. A reflective Tyvek coating lines the interior of the drum around the LED and a diffusive sheet of Teflon is placed across the drum opening. Pulsed light from the LED is reflected within the drum before escaping via the Teflon sheet, which provides an effectively uniform (within ∼3%) source of light due to its diffusive nature. The calibration is end-to-end and is derived from the individual pixel response to this uniform light, accounting for differences in light collection, quantum efficiency, pixel area and camera shadow.

The calibration of pixels is sometimes cross-checked through the firing of a nitrogen laser within a telescope's field of view [151]. As the laser's power is known and atmospheric effects are well understood, the amount of laser light reaching the fluorescence telescope may be estimated. This type of calibration has an uncertainty of 12% however, due to fluctuations in the atmosphere and the alignment of the test laser in the telescope's field of view.

Extensive air showers are identified by fluorescence detectors through a 4 level trigger. When the signal (integrated over 10 time bins to improve

signal to noise ratio) measured by a particular pixel exceeds a simple threshold the first level trigger is activated. This particular threshold is not fixed, and is continuously varied such that a first level pixel trigger rate of 100 Hz is achieved. The second level trigger searches for a pattern in the first level triggered FD pixels. Once 4 or 5 adjacent pixels with the first level trigger are identified within a time window of 1 to 32 μs, the second level trigger is activated. The rate of second level triggers is approximately 0.1 Hz per mirror. The final triggers check for a time structure within the identified event, and carry out a quick rudimentary reconstruction of the event to identify any data from the surface detector array that may be of interest.

2.2.2 Geometry

Reconstruction of the geometry of an event measured by a fluorescence detector is a two-step process. Firstly the shower detector plane[3] (seen in figure 2.14) must be identified, and secondly, the shower axis itself.
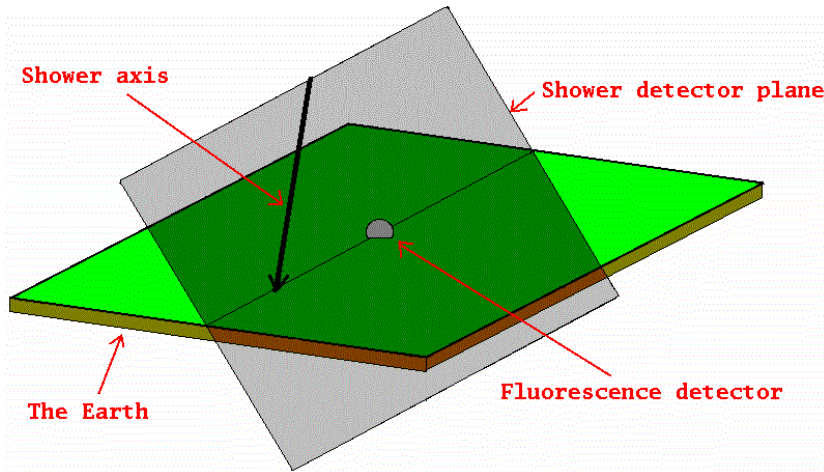

Figure 2.14: *The Earth, shower axis and location of detector with respect to the shower detector plane are demonstrated.*

The shower detector plane may be found through a minimization of the χ function in equation 2.12:

$$\chi = \sum_i w_i (\vec{r_i} \cdot \vec{n})^2 \tag{2.12}$$

---

[3]The plane defined by the shower axis and the detector itself.

where $\vec{r_i}$ is the pointing direction of triggered FD pixels, w_i is the associated weight assigned to that particular measurement, and $\vec{n}$ is the pointing direction of a vector normal to the shower detector plane.

Once the shower detector plane has been identified the shower axis geometry may be estimated. The arrival time $\hat{t}_i$ of light from a shower in the detector plane is described by equation 2.13 and figure 2.15:

$$\hat{t}_i = T_0 + \frac{R_p}{c} \tan\left(\frac{\chi_0 - \chi_i}{2}\right) \tag{2.13}$$

$\hat{t}_i$	Arrival time of light in pixel i	T_0	Time when shower is closest to FD
c	Speed of light in atmosphere	R_p	Core distance at time T_0
χ_0	Angle between shower axis and Earth	χ_i	Elevation of pixel i

NOTE:
This figure is included on page 50
of the print copy of the thesis held in
the University of Adelaide Library.

Figure 2.15: *Adapted from [91]. Demonstrating the geometry used in equation 2.13.*

A fit of equation 2.13 is performed with timing information from triggered FD pixels to estimate the free parameters T_0, R_p and χ_0. Within the shower detector plane the parameters R_p and χ_0 may successfully describe the position of the air shower axis.

Measurements from surface detectors (hybrid data) may be used to improve the reconstruction of the shower's geometry. If $\hat{t}_j$ is the expected arrival time of the shower at surface detector j, then:

$$\hat{t}_j = T_0 + \frac{\vec{R_j} \cdot \vec{S}}{c} \tag{2.14}$$

Where $\vec{R_j}$ is the vector between the fluorescence detector and surface detector j and $\vec{S}$ is a normalized vector along the shower axis. A fit of the data is performed by minimizing the sum of both the fitted equation 2.13 and 2.14 χ^2 values.

The accuracy of this approach is dependent upon having a wide variety of measurements however as seen in figure 2.16. The dashed line represents a good fit of equation 2.13 to data measured from a FD, and the solid line a good fit to hybrid FD and surface detector measurements. Both FD and hybrid are good fits to the measured data points, but there is a substantial discrepancy in the shape of the fit and hence fitted parameters T_0, χ_0 and R_p. The additional measurements from the surface detectors allow additional constraints to be placed upon the fit, and therefore a more accurate reconstruction of a shower's geometry to be made.

NOTE:
This figure is included on page 51
of the print copy of the thesis held in
the University of Adelaide Library.

Figure 2.16: *Taken from [91]. Black points describe measurements by the FD, while red points are measurements made by the surface detector array. The dotted line is the result of fitting equation 2.13 with just FD data, while the solid line is the result of a fit using surface detector data as well.*

2.2.3   Energy measurement

The energy of an extensive air shower may be estimated through measurements made by a fluorescence detector. Light from an extensive air shower received at a detector is indicative of the amount of energy deposited by that shower in the Earth's atmosphere. By integrating the total energy deposited by the shower, the energy of the initiating cosmic ray particle may

be estimated.

The first step is to calculate the total light flux from an air shower arriving at a fluorescence detector as a function of time. This is achieved by integrating the signal from triggered FD pixels within an angle zeta[4] of the location of the shower (estimated from the shower geometry), during 100 ns time periods. Uncertainties are assigned to these timebins based upon fluctuations of cathode photoelectrons and secondary electron emission within the dynode chain of the photomultiplier tubes [91]. New timebins, signals and associated uncertainties are then created by progressively integrating the signal from the shower until a minimum signal to noise ratio is exceeded. This has the effect of reducing the number of datapoints in the analysis, but improving their individual signal to noise ratio. The number of photons (370 nm equivalent) are then calculated using calibrations based upon studies using the 'illumination drum' mentioned in section 2.2.1. Currently the conversion from signal to number of photons has an uncertainty of around 10% [4]. An example of the signal vs time, and number of 370 nm equivalent photons vs time seen in an extensive air shower may be seen in figure 2.17.

NOTE:
This figure is included on page 52
of the print copy of the thesis held in
the University of Adelaide Library.

Figure 2.17: *Adapted from [91].* **[Left]** *Signal from an extensive air shower recorded by an FD vs time.* **[Right]** *Same air shower as seen on the left, but converted into number of photons arriving (timebins have not been combined).*

The amount of energy deposited (dE/dX_i) by an extensive air shower at a particular point i is approximately proportional to the number of electrons $N^{elect}(X_i)$ at that particular point, as seen in equation 2.15:

$$\frac{dE}{dX_i} = N^{elect}(X)\alpha_i \tag{2.15}$$

---

[4]The angle zeta is calculated uniquely for each shower based upon signal to noise ratios of the triggered FD pixels

where α_i is the average energy loss of an electron at point i and 'slant depth' X_i is a measure of atmospheric depth - that is, how far in the atmosphere has penetrated up to a particular point. Slant depth X_i for an extensive air shower is described by equation 2.16:

$$X_i = \frac{1}{\cos\theta} \int_{z_i}^{\infty} \rho(z)dz \qquad (2.16)$$

where z_i is the height of point i, θ is the shower's zenith angle, and $\rho(z)$ is the atmospheric pressure at a height z.

Light detected by the Auger fluorescence telescopes has its origin in both the fluorescence and Cherenkov light produced by an extensive air shower. Furthermore, Mie and Rayleigh scattering in the atmosphere attenuates the shower light flux before it reaches the telescope. In order to identify the number of photons originally created via nitrogen fluorescence at the shower track, this atmospheric attenuation must be accounted for, and any additional Cherenkov radiation subtracted from the measured signal.

Atmospheric monitoring with several weather stations, LIDAR and the CLF[5] provide information about the aerosol content of the atmosphere at different times during the night. With information about the shower's geometry, this allows the attenuation and scattering of fluorescence and Cherenkov light to be corrected for, and the number of fluorescence photons at the shower track to be estimated. The number of photons produced via fluorescence is proportional to the number of electrons at that point in the shower, and the average energy deposited by an electron α_i is known [171], therefore the energy deposited dE/dX_i may be estimated.

The limited field of view of the Pierre Auger Observatory's fluorescence detectors means that the shape of the shower's longitudinal profile must be extrapolated for those parts of the shower not directly seen by the detector. This is achieved through the fitting of a 'Gaisser-Hillas' function (equation 2.17), which has been found to describe the development of an extensive air shower quite well [82].

$$N(x) = N_{max}(\frac{x}{w})^w e^{w-x} \qquad (2.17)$$

$$\begin{aligned} x &= (X - X_0)/\lambda \\ w &= (X_{max} - X_0)/\lambda \end{aligned}$$

where X_0, X_{max} and λ are the fitted parameters. Figure 2.18 demonstrates measurements of energy deposited vs slant depth for an air shower measured by the Pierre Auger Observatory, along with the shape of a fitted Gaisser-Hillas function.

---

[5]Central Laser Facility

> NOTE:
> This figure is included on page 54
> of the print copy of the thesis held in
> the University of Adelaide Library.

Figure 2.18: *Adapted from [91]. Example of a measurement of energy deposit dE/dX vs slant depth for an extensive air shower measured by the Pierre Auger Observatory. The red line represents the shape of a Gaisser-Hillas function fitted to the measured data.*

The energy of the initiating cosmic ray is estimated by simply integrating the fitted Gaisser-Hillas for the measured air shower. Not all of the cosmic ray's energy is lost via the electromagnetic component of the shower however, therefore this integral is an underestimate. The energy lost to muons and neutrinos varies with both the energy of the initiating cosmic ray particle, the type of cosmic ray particle, and the hadronic interaction model used to describe the air shower [34]. A "missing energy" correction is therefore applied to estimates of cosmic ray energy. An example of an energy correction calculated from CORSKIA simulations is shown in equation 2.18 [170]:

$$\frac{E_{measured}}{E_{actual}} = (0.959 \pm 0.003) - (0.082 \pm 0.003)E_{measured}^{-(0.150 \pm 0.006)} \qquad (2.18)$$

where $E_{measured}$ is the energy measurement (in EeV) from the integrated longitudinal profile and E_{actual} is the actual energy of the cosmic ray particle.

Uncertainty in the final reconstructed shower energy is around 8% [12]. This is in account of uncertainties in the fitted Gaisser-Hillas function, light flux, geometrical reconstruction and estimation of the missing energy.

2.2.4   Mass composition

Mass composition analysis with fluorescence detector measurements is carried out through studies of the measured elongation rate. The elongation rate is the variation of the mean measured X_{max}[6] value with measured energy. X_{max} is a mass sensitive parameter, with showers initiated by heavier initial cosmic ray particles having a lower X_{max} value than lighter showers of equivalent energy. Shower-to-shower fluctuations make mass determination on an individual shower basis unreliable, but by comparing the measured mean X_{max} with the theoretical mean X_{max} values for different pure compositions, the general trend of mass composition with energy may be studied.

An extensive air shower initiated by an iron nucleus with energy 'E' is approximately equivalent to the superposition of 56 individual proton induced showers of energy 'E/56'. Therefore a set of iron nuclei induced showers at a particular energy are going to tend to develop higher in the atmosphere than a set of proton induced showers at that same energy. Thus the average X_{max} of the fitted Gaisser-Hillas function for a set of showers will decrease at a particular energy as the composition of that set tends towards a heavier composition.

Seen in figure 2.19 is an elongation rate plot presented by the Pierre Auger Collaboration in 2007. The mean reconstructed X_{max} values for high quality measurements of extensive air showers by fluorescence detectors are plotted as a function of energy. Along with the measured data are the Monte Carlo simulated mean X_{max} values for pure proton and pure iron compositions. If the Pierre Auger Observatory were to be measuring purely proton or iron nuclei initiated air showers, then the measured mean X_{max} values would be expected to be in agreement with one or the other of the simulated mean X_{max} values (multiple models are available as the high energy physics involved in cosmic rays require extrapolation of laboratory measurements at lower energies). A measured mean moving towards either the simulated purely proton or iron nuclei compositions indicates that the overall cosmic ray composition is becoming "lighter" or "heavier" respectively.

Another opportunity to study mass composition with fluorescence detector data is through the width of the measured X_{max} distribution at a particular energy. As an extensive air shower initiated by a heavier hadronic particle may be considered as a superposition of multiple proton initated showers of lower energy, the superposition acts to average out many of the fluctuations of the 'individual showers'. This results in less fluctuation between X_{max} values recorded by heavier showers at a particular energy than

---

[6]X_{max} is the depth at which a particular air shower has its maximum number of charged particles.

NOTE:
This figure is included on page 56
of the print copy of the thesis held in
the University of Adelaide Library.

Figure 2.19: *Figure taken from [5]. Atmospheric depth X_{max} of the shower maximum as a function of energy. The data points are accompanied by their statistical uncertainties and respective number of events in each bin. The energy-independent scale uncertainty in X_{max} is less than 15 g/cm^2. The expectations for primary protons and iron nuclei are shown for three different models.*

proton ones. Therefore for a mainly proton based composition a much wider distribution of X_{max} values would be recorded, than for a mostly iron nuclei one. A problem with this approach is that this concept of 'width' is ill-defined, as the width of a distribution of measured and simulated X_{max} values are non-symmetric.

Chapter 3

Recording cloud conditions

Clouds can seriously affect measurements made by the Pierre Auger observatory's fluorescence detectors. Nitrogen fluorescence and Cherenkov light produced by extensive air showers may be both scattered towards and away from fluorescence detectors, resulting in erroneous measurements of the development of that particular shower. In order to provide a record of cloud conditions above the observatory, Raytheon 2000B infrared cameras have been installed at each of the Auger fluorescence detector sites and set up to periodically record images of the sky within the field-of-view of their associated detectors. Cloud has a higher effective temperature than clear sky, therefore cloud and clear sky are usually able to be resolved within infrared images recorded of the night sky. Nitrogen fluorescence and Cherenkov radiation

3.1 Light from extensive air showers and clouds

Both nitrogen fluorescence and Cherenkov light from extensive air showers may be scattered by cloud, which influences the amount of light being measured by fluorescence detectors. If a bank of cloud happens to be present between an extensive air shower axis and fluorescence detector, then much of the fluorescence light from that shower will be scattered away before it can reach the detector - resulting in a dip in the measured fluorescence profile of that shower. Passing directly through a bank of cloud however, causes Cherenkov light (usually not directed towards the detectors) to be scattered towards a fluorescence detector, which will result in an apparent 'bump' in the longitudinal profile of that shower.

3.1.1   Nitrogen fluorescence

Nitrogen fluorescence is created through the excitation of electrons within atmospheric nitrogen molecules by the passage of an extensive air shower's particles. These excited electons subsequently decay down to a less energetic state, releasing this loss in energy as a photon. The resulting flux of fluorescence photons undergoes scattering and attenuation by aerosols in the atmosphere, which is corrected for through the use of measurements of atmospheric aerosol content and atmospheric models. If these photons pass through a bank of cloud however, they will suffer additional attenuation through Mie scattering that is currently not accounted for through existing corrections. The scattering process is demonstrated below, in figure 3.1.
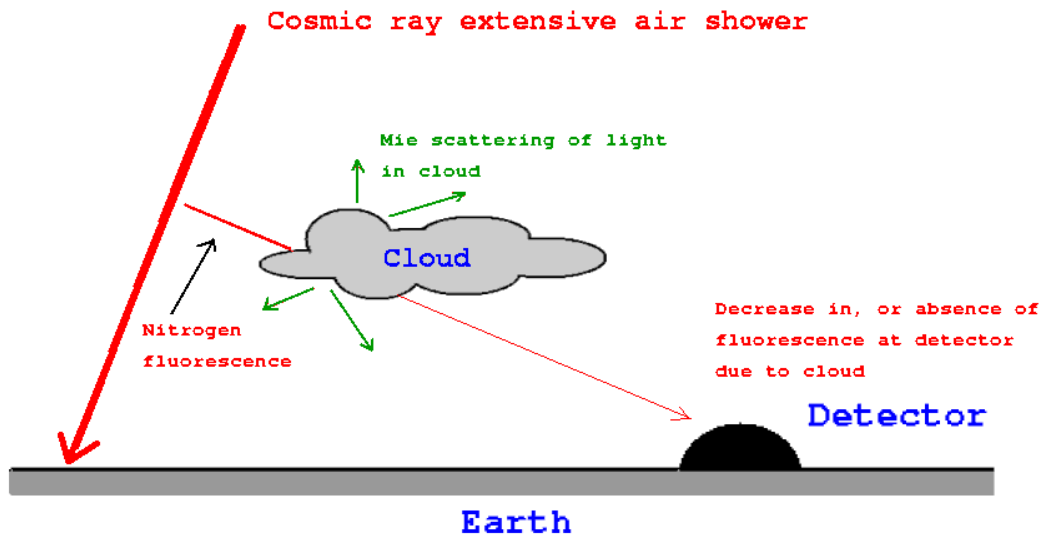

Figure 3.1: *Diagram showing how nitrogen fluorescence from an extensive air shower may be attenuated by cloud.*

This lack of correction manifests as a dip appearing within the measured longitudinal profile for that particular shower as additional photons are attenuated. An example of such a measured longitudinal profile may be seen in figure 3.2. A prominent dip in the profile characterized by a single measured point may be seen at a depth of approximately 860 g.cm^{-2}. The fitted Gaisser-Hillas function, in this case, is strongly influenced by this point, appearing to both underestimate the shower's energy and X$_{max}$ value. The strong weight assigned to this single point arises from the large number of timebins combined to create it. Sometimes dips do not appear in the longitudinal profile, despite the influence of cloud, when only the earliest or

later parts of the shower are obscured by cloud. This manifests as a shorter overall shower track length recorded by the detector.
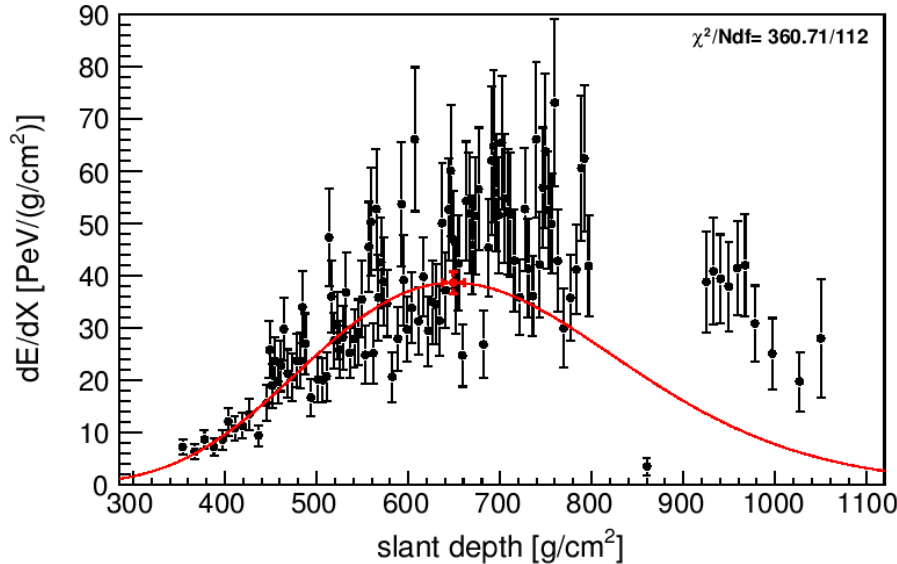

Figure 3.2: *Example of a measured extensive air shower, where ultraviolet light has been scattered away from a fluorescence detector as a result of passing through a bank of cloud. The solid line indicates the Gaisser-Hillas fit by the Auger analysis program.*

3.1.2 Cherenkov light

Photons from extensive air showers may be scattered towards Auger fluorescence detectors by cloud, resulting in an excess over the level of light that should be measured. Cherenkov light produced by extensive air showers is emitted in a cone-like front directed along the shower axis, and is normally not detected by fluorescence detectors. Upon encountering a bank of cloud however, a significant amount of this Cherenkov light can be scattered towards, and observed by Auger fluorescence detectors.

Cherenkov light is created when charged particles travel faster than the phase velocity of light in a dielectric medium. The electromagnetic field of charged particles in the extensive air shower polarize and atmospheric atoms as they travel. As the atmospheric electrons return to their unpolarized state, photons of light are emitted. If the shower electrons are travelling fast enough (minimum energy of 21 MeV at sea level [89] which increases with

altitude) then these photons will constructively interfere - travelling in a cone-like shape along the shower's axis. As the shower develops the intensity of the Cherenkov light cone will increase as the photons are constantly being produced, yet are not travelling fast enough to pull ahead of the shower front. Unless the extensive air shower in question is travelling directly towards a fluorescence detector, very little of this Cherenkov light will ordinarily be detected.

The droplets of water that make up cloud can have a similar radii size (order of μm) to the wavelength of Cherenkov light produced by extensive air showers. Therefore shower Cherenkov light will undergo Mie scattering while passing through banks of cloud. Some Cherenkov light will be scattered towards the Auger fluorescence detectors as demonstrated in figure 3.3.
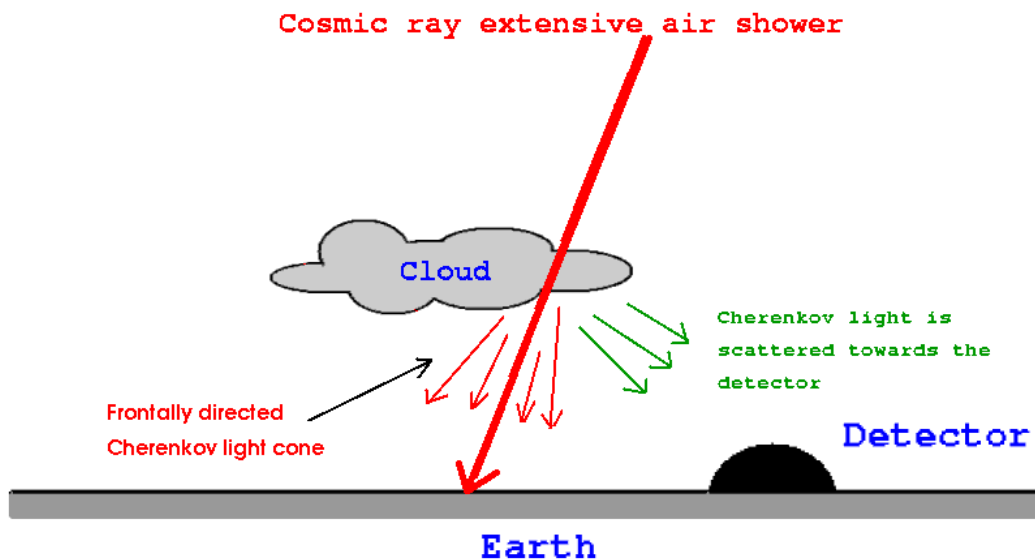

Figure 3.3: *Diagram showing how Cherenkov light can be scattered by cloud towards a fluorescence detector.*

This extra Cherenkov light will be detected by the fluorescence detector along with any fluorescence produced by the shower, and will manifest as a peak in the reconstructed longitudinal profile. An example may be seen in figure 3.4 where a longitudinal profile measured by the Los Morados fluorescence detector is displayed. A clear bump in the reconstructed shower profile is seen at a depth of approximately 670 g.cm^{-2}. Depending upon a bump's location and size, the Gaisser-Hillas function fitted to a profile may be influenced by the extra Cherenkov light, resulting in a less accurate reconstruction of the shower's energy and X$_{max}$ value.
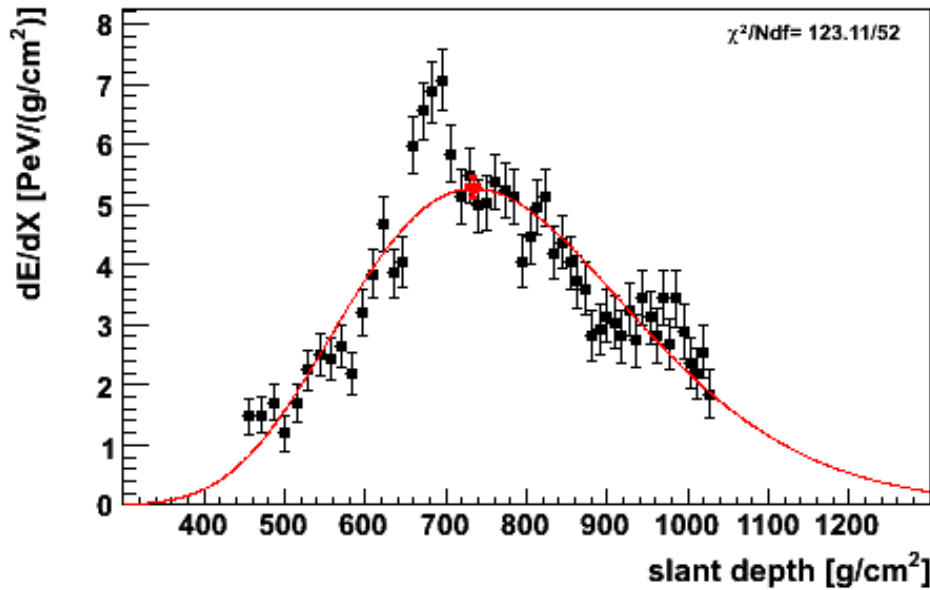
Figure 3.4: *Example of a measured extensive air shower where extra light has been scattered towards a fluorescence detector as a result of passing through a bank of cloud.*

3.2 Night sky radiation

Radiation from the Earth's atmosphere is known as atmospheric emission [104]. Atmospheric emission is the result of infrared radiation emitted by certain gases (such as water vapor, carbon dioxide and ozone) being heated by radiation emitted by the Earth or Sun. For the temperatures involved, such radiation is predominently in the infrared 4-50 μm band. By volume, approximately 1% of the gases in the Earth's atmosphere are responsible for the majority of the atmosphere's radiative power. Overall, the strength of the atmospheric radiation depends upon atmospheric temperature and the concentrations and distributions of radiative gases in the atmosphere at a particular time. Due to their high water vapor content, banks of cloud are optically thick and radiate as a black body at the temperature of the surrounding atmosphere.

3.2.1 Clear night sky

Radiation from a clear night sky may simply be taken as the integral of the radiative contributions from many atmospheric layers. While all layers have some contribution to the overall flux measured at ground level, most

($\approx$72%) [163] atmospheric emission originates within the lowest 100m of the atmosphere and $\approx$90% within 600m above the Earth's surface [85].

The luminosity of atmospheric emission for an observer on the Earth's surface is the combination of the emission from many different atmospheric layers at different temperatures. By treating each atmospheric layer as a black body emitter with a temperature T and a transmittance T_r for that layer, then the total atmospheric emission at a wavelength λ may be described as a sum of these layers, as seen in equation 3.1:

$$L_\downarrow(\lambda) = \int_\tau^1 B(\lambda, T).dT_r \tag{3.1}$$

where $L_\downarrow(\lambda)$ is the radiance of the atmosphere for a ground observer, τ is the total transmittance of light from the highest layer of the atmosphere being considered, T_r is the total transmittance for light produced at a particular layer of the atmosphere and $B(\lambda, T)$ is the average black body radiance of the atmosphere at a wavelength λ and temperature T as seen below in equation 3.2:

$$B(\lambda, T) = \frac{2hc^2}{\lambda^5} \frac{1}{\exp(\frac{hc}{\lambda kT}) - 1} \tag{3.2}$$

where h is Planck's constant, c is the speed of light and k is the Boltzmann constant.

Calculation of the total transmittance T_r for light of a particular wavelength originating from a particular height requires knowledge of the amount of atmosphere being traversed, the extent of scattering from aerosols, and scattering and absorption by atmospheric molecules. These are all factors that require knowledge of the physical properties of the atmosphere at that particular time. Scattering by atmospheric molecules may be accounted for through the use of Rayleigh scattering theory, and aerosols through Mie scattering theory, but molecular absorption is more complicated due to variations with gas pressure and temperature and may require the use of spectroscopic databases such as HITRAN [158] and are typically computationally expensive to calculate.

A simpler, empirical way of expressing the atmospheric emission of a clear sky is by approximating the night sky as a grey (equation 3.3) or black body (equation 3.4) radiator [147]:

$$R_{sky} = \sigma \epsilon T_{ambient}^4 \tag{3.3}$$
$$R_{sky} = \sigma T_{sky}^4 \tag{3.4}$$

where R_{sky} is the flux of atmospheric emission, σ is the Stefan-Boltzmann constant, T_{sky} is the effective blackbody temperature of a clear sky at the

zenith, and ϵ is the effective emissivity of the atmosphere if it is considered to be a grey body at the ambient temperature $T_{ambient}$. In these models, parameterizations are developed for ϵ and T_{sky} as a function of measurable ground level weather parameters such as water vapor pressure or the ambient temperature.

These parameterizations are developed through the fitting of simulated or independently measured data to different functional forms obtained experimentally or theoretically. Such functional forms usually predict emissivity or effective clear sky temperature as a function of ground level ambient temperature T (in Kelvin), water vapor pressure e_0 (in mb), or dew point temperature T_{dp} (in °C). Often such parameterizations were only calculated using a limited range of experimental data, at specific wavelengths, averaged over different areas of sky or were fitted to data only gathered at specific locations, and so cannot be expected to perform well at a different geography or climate. Some examples of these parameterizations may be seen below:

$\epsilon(e_0)$	$=$	$0.0746 + 0.0066e_0$	Efimova (1961) [70]
$\epsilon(T)$	$=$	$9.365\text{x}10^{-6}T^2$	Swinbank (1963) [172][141][68]
$\epsilon(e_0, T)$	$=$	$1.24(e_0/T)^{1/7}$	Brutsaert (1975) [46]
$\epsilon(T_{dp})$	$=$	$0.787 + 0.764\ln[(T_{dp} + 273)/273]$	Clark et al. (1978) [57]
$T_{sky}(T)$	$=$	$-22.6 + 1.12T$	Maghrabi (2007) [130] (Temp in °C)
$T_{sky}(e_0)$	$=$	$-33.1 + 8.6\sqrt{e_0}$	Maghrabi (2007) [130]
$T_{sky}(T, e_0)$	$=$	$-30.7 + 4.12\sqrt{e_0} + 0.78T$	Maghrabi (2007) [130] (Temp in °C)

3.2.2 Cloud

The optical thickness of clouds (due to their water vapor content) means they are effective black bodies, and thus radiate relatively strongly in the infrared and microwave portion of the electromagnetic spectrum [95]. In cloudy conditions, equation 3.1 therefore becomes equation 3.5, which takes into account the contribution from the cloud:

$$L_{\downarrow}(\lambda) = \int_{\tau}^{1} B(\lambda, T).dT_r + B_{cloud}(\lambda, T_{cloud})\tau \qquad (3.5)$$

where τ is the total transmittance from the height of the cloud, $B_{cloud}(\lambda, T_{cloud})$ is the flux of light from the cloud at a wavelength λ and a cloud base temperature T_{cloud}. The contribution to infrared atmospheric emission by cloud increases at lower cloud altitudes due to increased total emissivity (less atmospheric attenuation) and higher effective cloud base temperature due to increased proximity to the Earth's surface [119].

NOTE:
This figure is included on page 64
of the print copy of the thesis held in
the University of Adelaide Library.

Figure 3.5: *Adapted from [130]. MODTRAN simulated infrared spectrum for cloudy and clear skies at the zenith angle (T_{air} = 21°C, RH=75.9% and the PMV=1 cm). [**Red**] Clear skies. [**Blue**] High altitude cirrus cloud. [**Pink**] Low altitude stratus cloud.*

This may be seen in figure 3.5 where MODTRAN has been used to simulate infrared radiation spectra for a clear and cloudy night at a zenith angle of 0°. The red line corresponds to the spectrum simulated for a clear sky, and roughly corresponds to the emission spectrum of a blackbody object close to the ambient temperature at wavelengths below 8μm and above 23μm. Absorption and emission by atmospheric water vapor, carbon dioxide, ozone and methane is primarily responsible for the shape of the spectrum in between. Simulated atmospheric emission by high altitude cirrus clouds is represented by the blue line and corresponds very closely to the spectrum

simulated for clear skies. This is due to the lower temperature of high altitude cloud and substantial airmass between the observer and the cloud. The pink line represents the simulated emission of low altitude stratus cloud which corresponds to the blackbody emission of an object close to the ambient temperature, due to the higher cloud temperature close to the ground and decreased air mass between the cloud and an observer.

The cloud base temperature is difficult to measure directly but has been estimated in the past [150][113] through the use of equation 3.6:

$$T_{cloud} = T_{air} - L.Z_{cloud} \tag{3.6}$$

where T_{cloud} is the estimated cloud base temperature, T_{air} is the ground level ambient temperature, Z_{cloud} is the cloud height and L is the temperature lapse rate (such as a standard lapse rate of 6.5 °C.km^{-1}).The lapse rate is not always constant at different altitudes, therefore this approximation tends to break down for higher altitude cloud.

In addition, the atmosphere may contribute to the effective measurable temperature at ground level, particularly if the cloud is some distance away from the observer (being at a high altitude, or being viewed at a nonzero zenith angle). The temperature may also vary according to the amount, and the type of cloud present [85][163]. A suggested approximation [130] for an overcast sky effective temperature is equation 3.7:

$$T_{sky} = a + bT_{cloud} + cT_{air} + d\sqrt{\epsilon_0} \tag{3.7}$$

where T_{sky}, T_{cloud}, T_{air} are the effective sky, cloud base and ambient temperatures respectively, $a/b/c/d$ are fitted parameters and ϵ_0 is the measured water vapor pressure at ground level.

Cloud base height may be estimated through equation 3.6, by assuming cloud formation at a height where the atmospheric temperature is equal to the dewpoint temperature, as seen in equation 3.8:

$$Z_{cloud} = \frac{T_{air} - T_d}{L} \tag{3.8}$$

where T_d is the dew point temperature. This approximation assumes a constant lapse rate however, and so tends to break down when trying to predict very high cloud altitudes.

3.2.3 Zenith angle dependence

The effective sky temperature varies with zenith angle even in a completely cloud-free sky. A clear sky appears at its coolest directly overhead an Earthbound observer, and progressively increases in effective temperature with

zenith angle until it appears to radiate as a blackbody at ambient temperature at low elevation levels.

Atmospheric water vapor has a very high emissivity. Therefore an increase of water vapor within a line of sight will substantially increase the amount of radiation being received [68]. Most of the atmosphere's water vapor content is located relatively close to the Earth's surface. An increasing zenith angle will therefore increase the amount of water vapor, and thus emitted radation.

The radiative emission from a sample of water vapor varies as the logarithm of the optical depth of that water vapor [72][152][153]. Maghrabi [130] suggests that this may be interpreted as a variation of effective clear sky temperature with the natural logarithm of $sec(\theta)$ as seen in equation 3.9 [130]:

$$T_{sky(\theta)} = A + Bln(sec(\theta)) \tag{3.9}$$

where A and B are fitted parameters and θ is the zenith angle. Maghrabi [130] suggests that the equation may be used to describe the variation of effective clear sky temperature with zenith angle by fitting it with predicted clear sky temperatures at a zenith angle of 0° and the ambient temperature at an elevation of 87°. Variation of the effective temperature of clouds on overcast days may also be approximately described by equation 3.9.

Figure 3.6 demonstrates this increase in radiation with zenith angle. In the left-most plot are measurements made of the effective sky temperature of a clear sky at different zenith angles by a single pixel radiometer. With increasing zenith (looking closer and closer towards the horizon) angle the effective temperature of the sky increases at an increasing rate. On the right may be seen an infrared picture taken of a clear night sky and horizon. Close to the horizon the radiance of the night sky may be observed to increase through a distinct glow - appearing brighter than the rest of the night sky, due to the increased air and water vapor mass being observed by the infrared camera.

NOTE:
This figure is included on page 67
of the print copy of the thesis held in
the University of Adelaide Library.

Figure 3.6: *[**Left**] Adapted from [130]. Illustrating variation of clear sky effective temperature with zenith angle. Measurements were made with a single pixel radiometer with a bandpass from 5.5 to 20 μm. The ambient temperature, water vapor pressure and dew point temperature were 13.8 °C, 10 mb and 6.8 °C respectively. [**Right**] Picture of a clear sky taken by an infrared camera at Los Leones. A small piece of cloud in the distance can be seen near the horizon. The signal recorded for the sky increases the closer one gets to the horizon, despite the lack of cloud in that area.*

3.3   Raytheon 2000B infrared camera

The Raytheon 2000B infrared camera has been chosen to provide a record of cloud conditions around the Pierre Auger observatory. The camera's operation is based upon the pyroelectric effect, which means while the camera is good at resolving objects of differing temperatures, it has difficulty in providing quantitative information about scenes of uniform temperature (such as completely clear and overcast nights). Four cameras have now been purchased and have been successfully installed at each of the fluorescence detector sites at the Auger South array in Argentina.

3.3.1   Technical details

All four cloud cameras are non-radiometric - that is, there is no direct relationship between the signal registered by the camera and the temperature of whatever object that camera is looking at. Pixels within the camera are made up of a pyroelectric[1] material sandwiched in a capacitor-like arrangement. Modulation of incident radiation upon each pixel creates a signal that depends upon the subsequent induced modulation of the temperature in that pixel. The sensitivity of the camera pixels depends upon the rate-of-change of both the pixel's permittivity and polarization, therefore sensitivity may be modified through the composition of the pyroelectric material and the addition of an external electric field. Each of the camera's 76800 pixels are assembled within an array and have their incident radiation modulated through the use of a spinning chopper wheel in front of the array. The chopper consists of a Germanium wheel of alternating BDO (binary diffractive optic) and planar regions arranged in a Archimedes spiral pattern. The final signals recorded are the result of the difference between signals registered by pixels after being exposed to different regions of the chopper wheel.

Consider a single pixel within the infrared camera. It is a rectangular block of pyroelectric Barium Strontium Titanate with a polarization $P(T)$ that depends upon that pixel's temperature. Maxwell's equations with Gauss' law suggests equation 3.10:

$$D = \epsilon.E + P(T) = \frac{Q(T)}{A} \tag{3.10}$$

where D is electric displacement, T is the pixel's temperature, ϵ is the dielectric permittivity, E is the electric field strength, Q is the total surface charge of the pixel and A is the total pixel surface area.

---

[1]A pyroelectric material is a material (Barium Strontium Titanate in this case) that has its intrinsic electric polarisation depending upon the temperature of that material.

Treating the pixel as a capacitor (with capacitance C) reveals a voltage V across it, as seen in equation 3.11.

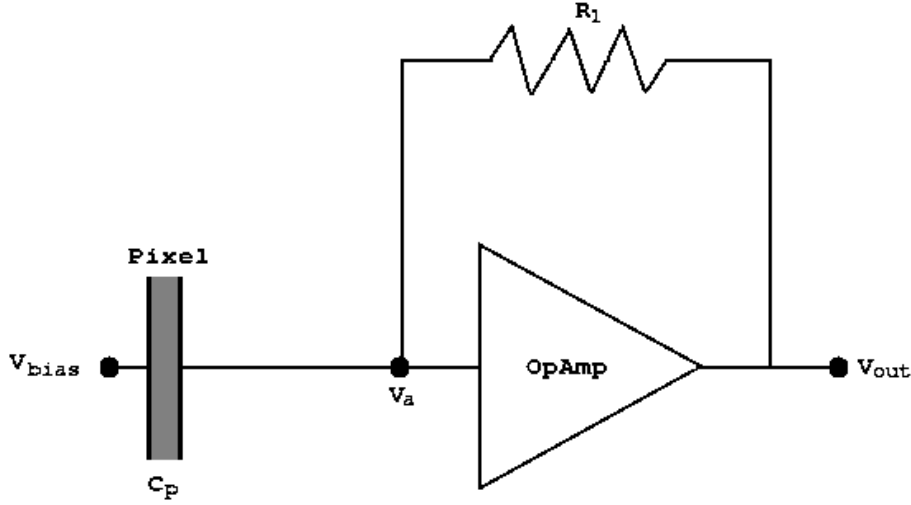$$V(T) = \frac{Q(T)}{C} = \frac{A}{C}(\epsilon.E + P(T)) \tag{3.11}$$

Figure 3.7: *Diagram showing how current generated from a pixel is converted to a voltage signal by a differentiator. The capacitor C_p is represents a pixel in our camera. The voltage V_a is held at ground i.e. 0 volts by the operational amplifier. R_1 is the feedback resistor, typically $10^{11} - 10^{12}\Omega$. V_{bias} is the voltage across the capacitor. V_{out} is the final pixel signal voltage.*

The voltage measured across the pixel is temperature dependent due to the temperature dependence of the pixel's polarization component. This voltage is converted into a signal V_{out} through the use of a differentiator seen in figure 3.7. V_a is held at 0V by the operational amplifier, therefore the voltage at V_{bias} is equivalent to the potential difference across the capacitor (the camera pixel) C_p. There is no current flowing from the operational amplifier, while the currents flowing via the resistor R_1 and capacitor are $\frac{V_{out}}{R_1}$ and $C_p \frac{dV_{bias}}{dt}$ respectively. Kirchoff's current law indicates that the sum of currents into V_a is zero, thus the final output signal V_{out} of a camera pixel depends upon the rate of change of voltage across the capacitor as shown in equation 3.12.

$$V_{out} = -R_1 C_p \frac{dV_{bias}}{dt} \tag{3.12}$$

The rate-of-change of voltage across the pixel depends upon the rate-of-change of temperature within that pixel (as temperature affects polarization). Sensitivity of the rate-of-change of voltage depends upon a few factors and should ideally be optimized for the maximum signal response. Taking the differential of the pixel's electric displacement $D(E, T)$ reveals equation 3.13, from which follows equation 3.14.

$$dD = \left(\frac{\partial D}{\partial T}\right)_E . dT + \left(\frac{\partial D}{\partial E}\right)_T . dE \qquad (3.13)$$

$$\left(\frac{\partial E}{\partial T}\right)_D = -\frac{\left(\frac{\partial D}{\partial T}\right)_E}{\left(\frac{\partial D}{\partial E}\right)_T} = -\frac{1}{\epsilon}\left(\frac{\partial P}{\partial T}\right)_E \qquad (3.14)$$

The response of the electric field within the camera pixel (and so hence V_{bias}) is proportional to the rate-of-change of polarization with temperature and is inversely proportional to the pixel's dielectric permittivity. Thus to maximize sensitivity the dielectric permittivity must be minimized and $\frac{dP}{dT}$ maximized.

NOTE:
This figure is included on page 70
of the print copy of the thesis held in
the University of Adelaide Library.

Figure 3.8: *A plot showing the relationship between spontaneous polarization, dielectric permittivity and temperature for Barium Strontium Titanate. The critical temperature T_c is approximately $22°C$. Taken from [92]*

Figure 3.8 shows the variation of relative permittivity (directly proportional to dielectric permittivity ϵ) and polarization with temperature. Above the critical temperature T_c, the spontaneous polarization related to temperature begins to level out (decreasing $\frac{dP}{dT}$) while the permittivity peaks and begins to decrease. Below T_c the rate-of-change of polarization with temperature also starts to level out and the relative permittivity approaches its minimum. Thus to maximize sensitivity, the pixel must be operating at, or below T_c, because it is here that $\frac{dP}{dT}$ is at its maximum and ϵ at its minimum. This critical temperature T_c corresponds to a phase transition within the Barium Strontium Titanate and may be adjusted by varying the Barium to Strontium ratio during pixel fabrication. In the case of the cloud cameras, T_c has been chosen to be close to the expected operating temperature ($20°C$) to maximize sensitivity. Sensitivity may also be increased (only in a limited fashion due to parasitic capacitance) through the addition of an external electric field which will suppress the dielectric permittivity, but it is not clear whether such a system was built into operation of these particular infrared cameras.
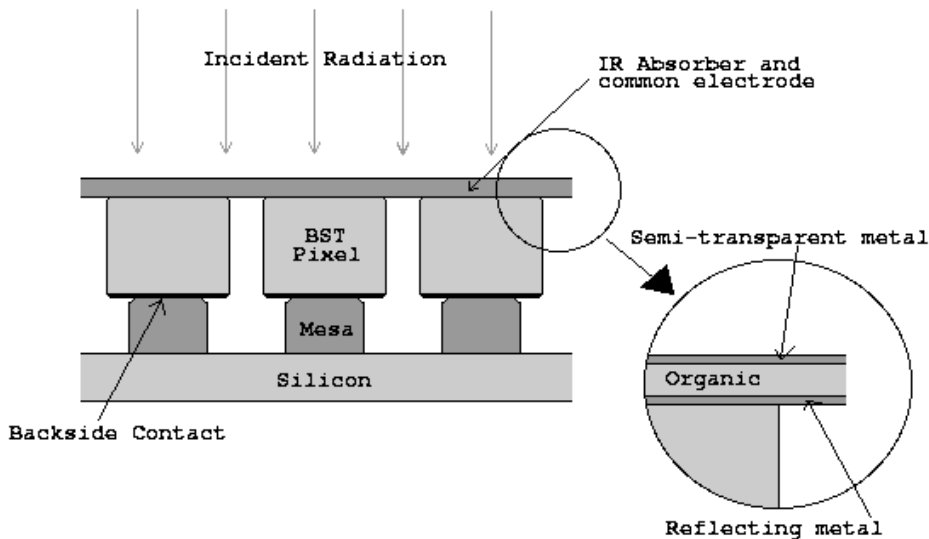

Figure 3.9: *Diagram showing the structure of the camera around each pixel.*

Barium Strontium Titanate is a very poor absorber of infrared radiation. Each pixel is therefore coated with a strong infrared absorbant substance - to such a thickness as to encourage destructive interference of any incident infrared radiation. This gives each pixel better than a 90% average absorption in the $7.5 - 13\mu$m range. Each pixel is mated to a silicon

circuit board by an organic mesa, as shown in figure 3.9. This mesa attempts to thermally isolate each pixel from other pieces of hardware within the camera. With no thermal isolation, thermal cross-talk between pixels would result in a 'blurring' effect in images recorded by that camera - as the temperature 'meant' to be recorded is suppressed when heat either bleeds out or in from neighbouring pixels. In front of the pixel array is an infrared lens with an effective focal length of 18mm. In front of the lens is an anti-reflection coated Germanium window that only allows transmission of light in the $7.5 - 13\mu$m spectral band. The lens focusses infrared light from the scene onto the camera's 240x320 array of pixels.

As noted above, between the lens and pixel array is an anti-reflection coated Germanium chopper wheel. The chopper wheel consists of alternating binary diffraction optic (BDO) and planar regions within the Germanium in an Archimedes spiral pattern, spinning 30 cycles per second. Planar regions of the chopper transmit an undistorted image of the scene, while the BDO regions transmit a distorted, effectively local average of the scene's infrared intensity. While the chopper is spinning, the Archimedes' spiral pattern approximates (see subsection 3.5.2) a straight edge (between planar and BDO regions) moving across the pixel array.

Being exposed periodically to different intensities of radiation results in a heating and cooling cycle in each pixel, whereby it will modulate between two different temperatures. This instigates the flow of charge responsible for creating a signal. While a particular pixel is receiving light transmitted through a planar chopper region it is said to be 'open', and while receiving light via the BDO region it is said to be 'closed'. The signal registered by a pixel (the V_{out} in figure 3.7) is sampled by the camera immediately prior to switching to 'open' from 'closed' and 'closed' from 'open'. The signal will be strongest (but also most unstable) immediately after switching 'open' to 'closed' or 'closed' to 'open' because it is at this point that the pixel is at the temperature furthest from its new goal and thus is going to be changing the fastest. The signal is sampled near the end of the cycle (as opposed to its strongest point at the start) because, at its strongest, it is also changing the most rapidly. Unless the signal is sampled at 'exactly' the same time in each of the heating/cooling samples, the fluctuations in signal will be much larger than if it is measured later in the cycle when the rate-of-the-rate-of-change of temperature is less. The 'closed' signal is subtracted from the 'open' signal to create the final signal output by the camera for a pixel. This operation has the added benefit of removing any signal offset introduced by the camera's electronics.

3.3.2 Camera setup

Raytheon 2000B infrared cameras have been installed at each fluorescence detector at the Pierre Auger observatory. Each camera has been configured to record cloud conditions during operation of each associated fluorescence detector. Camera normalization is carried out remotely every several months, to ensure uniformity in effective gain for pixels within each camera. Images recorded by the cameras are stored onsite and are either downloaded or physically carried back to Adelaide University for analysis. The Loma Amarilla cloud camera is unique however, in that it has a single pixel radiometer attached - providing a means for comparison between camera signal and actual effective sky temperature during camera operation.

Infrared cameras at each of the fluorescence detectors (FDs) have been set up to provide a record of cloud conditions within the field of view of that FD. Each cloud camera is mounted within a protective weather shield that is, in turn, mounted upon a pan-and-tilt device (seen in figure 3.10). The whole apparatus is controlled automatically from a local computer located within the FD building itself. During FD operation, each camera scans and takes five pictures across the FD detector's field of view every five minutes. Every fifteen minutes, in order to provide a general record of cloud conditions, each camera scans around and takes a total of twenty seven images above and around the FD, which are subsequently combined into a mosaic (see figure 3.10 for examples of mosaics and field of view scans). Images taken by the camera deliberately overlap, as lack of precision in the pan-and-tilt device means cameras can sometimes take pictures up to a degree away from the desired pointing direction. The overlap ensures that no information is lost and the actual pointing of each recorded is recorded precisely to well within a degree using a potentiometer.

Normalization of each camera is necessary due to the non-uniformity in the gain of pixels in each camera. Slight differences in size, chemical composition and any number of other variables mean that each pixel in each infrared camera has a slightly different response during camera operation. Without normalization, images taken by the camera will appear noiser than they otherwise could be. For an un-normalized image being taken of an isothermal scene, a variation of $\approx 3\%$ ($\frac{\sigma}{mean}$) will be measured, while normalized that same scene will have a variation of only $\approx 1\%$ [65]. In the case of the Raytheon 2000B infrared cameras, normalization takes place by assigning a corrective factor k to each pixel, as seen in equation 3.15:

$$k = \frac{N}{g} \qquad (3.15)$$

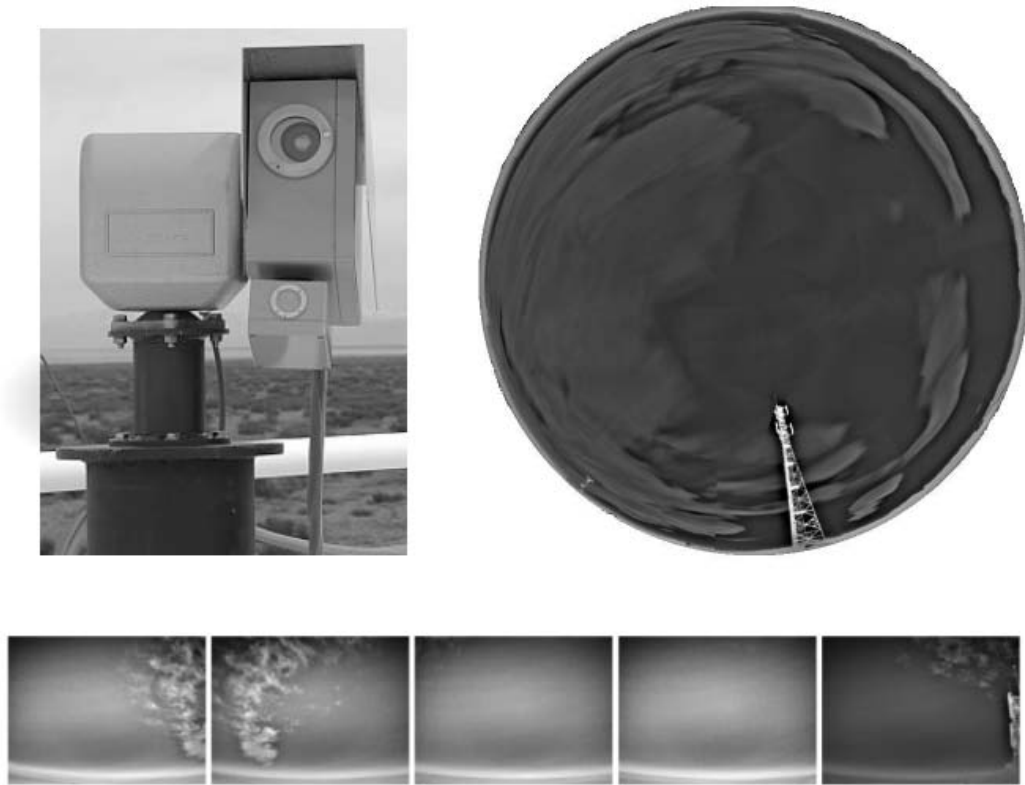where N is some arbitrary number the output of each pixel is being normal-

Figure 3.10: *[Top] A photo of the Raytheon Control IR 2000B camera installed at Loma Amarilla. The camera is mounted and sealed within a protective box (the larger of the two), observing the sky through an IR transparent weather shield. In this picture, a smaller radiometric thermopile can be observed to be attached below the main box, this is unique to the camera at the Loma Amarilla site and has not been installed on the cameras at the other sites. The whole apparatus is attached to a computer controlled pan-and-tilt device, to enable the camera to be pointed in nearly any direction. [Top right] An example of a mosaic of 27 images captured by the camera every 15 minutes, to provide a record of overall cloud conditions around the site. [Bottom] An example of the 5 images captured by the camera every 5 minutes across a fluorescence detector's field-of-view, these images overlap to some degree to ensure the image sequence always covers the entire field-of-view.*

ized to, and where g is the actual (un-normalized) response of a particular pixel.

This is accomplished by pointing the camera at an isothermal scene - where the scene average and scene temperature are identical for each pixel (and hence response). The corrective factor k (in equation 3.15) is then worked out by assigning an arbitrary number to N. Thus the response of each pixel will be an identical N whenever an isothermal scene of that particular temperature is viewed. In the case of the cloud cameras, normalization is carried out every several months by pointing the camera directly overhead the FD site on a completely clear night. As the effective temperature of clear sky varies roughly as $ln(sec(\theta))$ (where θ is the zenith angle), so the variation of temperature direction overhead is less than 2 degrees celsius within a zenith angle of 30 degrees. Thus clear sky above the fluorescence detector approximates an isothermal scene which is used to normalize each of the cloud cameras.

Images that are recorded, are losslessly compressed and written to a special file format created by Dr Andrew Smith. Along with the images themselves, other variables are recorded, such as the pointing direction of the image and the time of day each particular picture was taken. Given the enormous quantities of images that have to be recorded and stored, this is a simple and effective way to both store and access the data recorded by the cloud cameras. The ambient temperature and effective temperature of the sky is also recorded in the case of the Loma Amarilla cloud camera. A single night's worth of data from a single camera (after been fully compressed) requires approximately 85 MB of disk space for storage.

The cloud camera installed at Loma Amarilla is unique in that it has had a single pixel radiometric infrared thermopile attached to it. The thermopile records both the effective temperature of the piece of sky in the centre of any image taken by the camera, and the ambient temperature in the thermopile during the taking of that image. This allows direct comparison between the signal being reported by a cloud camera and the actual effective temperature of the sky the camera is looking at.

3.4 Camera signal and the night sky

When an image is recorded by a Raytheon 2000B infrared camera, each pixel within that image is assigned a signal depending upon the temperature and structure of the image scene. The cloud cameras are non-radiometic, meaning there is little direct relationship between temperature and the signal output by the camera - however there does exist a relationship between signal and

the *difference* in scene temperature and local camera temperature.

The signal (S) recorded by each pixel in both the open and closed chopper phases depends upon the difference in surface charge, and thus polarization within that pixel in both phases. Assuming a linear relationship between a pixel's polarization and its temperature, the signal recorded by a pixel will be therefore proportional to the difference in temperature of the pixel in its open phase (T_{open}), and the temperature in its closed phase (T_{closed}) i.e.

$$S \propto T_{open} - T_{closed} \tag{3.16}$$

In reality the overall relationship between polarization and temperature is non-linear (see figure 3.8), but given that the camera's pixels are only going to be fluctuating over a limited range of temperatures, this approximation may hold.

Assuming that each pixel is an effective blackbody radiator, is thermally insulated and that each reaches thermal equilibrium during both chopper phases, then the temperatures (T_{open} and T_{closed}) of each pixel will be:

$$T_{open} = \sqrt[4]{\epsilon_{open} T_{chop}^4 + (1 - \epsilon_{open}) T_{sky}^4} \tag{3.17}$$

$$T_{closed} = \sqrt[4]{\epsilon_{closed} T_{chop}^4 + (1 - \epsilon_{closed}) T_{ave}^4} \tag{3.18}$$

ϵ_{closed}	chopper emissivity (closed)	ϵ_{open}	chopper emissivity (open)
T_{chop}	temp. of chopper	T_{sky}	temp. of sky
T_{ave}	scene averaged effective temp.		

Thus according to equations 3.16, 3.17 and 3.18, the signal registered by a pixel must be approximately proportional to:

$$S \propto \left(\sqrt[4]{T_{sky}^4 + \epsilon_{open}(T_{chop}^4 - T_{sky}^4)} - \sqrt[4]{T_{ave}^4 + \epsilon_{closed}(T_{chop}^4 - T_{ave}^4)} \right) \tag{3.19}$$

Equation 3.19 may be further simplified with a Taylor expansion (around ϵ_{closed} and ϵ_{open}) if it is assumed that the pixel is viewing an isothermal scene, such that $T_{ave} = T_{sky}$, as seen in equation 3.20:

$$S \propto T_{sky} \left(\frac{1}{4} x (\epsilon_{open} - \epsilon_{closed}) - \frac{3}{32} x^2 (\epsilon_{open}^2 - \epsilon_{closed}^2) + ... \right) \tag{3.20}$$

$$\text{where} \quad x \quad = \quad (T_{chop}^4 - T_{sky}^4)/T_{sky}^4$$

As both ϵ_{open} and ϵ_{closed} are unknown variables within the camera, it may be useful to construct a parameterization such that:

$$S = A + T_{sky} \sum_{i=1}^{\infty} B_i x^i \tag{3.21}$$

where A and B_i are fitted constants. As i increases, B_i approaches zero, therefore it is expected only a limited number of values of B_i will have to be fitted for to create a good parameterization.

The effective temperature of a cloudy fragment of sky is approximately a combination of the radiation seen in clear sky and the radiation from a fragment of cloud. The effective temperature of cloudy sky T_{cloudy} is seen in equation 3.22:

$$T_{cloudy}^4 = T_{clear}^4 + T_{cloud}^4 \tag{3.22}$$

where T_{clear} and T_{cloud} are the effective temperatures of a clear night sky and the actual blackbody temperature of the cloud respectively.

The variable T_{ave} is the effective temperature of the sky seen by a pixel through the Germanium chopper wheel. The exact nature of the diffusion of light through the chopper wheel has not been investigated in this study, however for an isothermal scene, T_{ave} may be taken simply as T_{clear} on a clear night or T_{cloudy} in equation 3.22 on a cloudy night.

The low emissivity of the chopper wheel and its constant rotation suggests that conduction of heat to and from the surrounding air is its dominant cooling/heating mechanism. Therefore its temperature will be approximately that of the air surrounding the chopper wheel within the weather box housing the camera. Figure 3.11 indicates temperatures recorded within the Loma Amarilla cloud camera box and the average ambient temperature measured at the same time. Above an ambient temperature of 268 Kelvin there is an approximately constant offset of 6.8 degrees, indicating that air within the camera box is, on average, nearly 7 degrees warmer than the air outside the box. A Gaussian function describes the differences between the two temperatures well, suggesting that this is a systematic effect likely due to heat generated by the camera's electronics. The primary deviation from the Gaussian fit occurs at just below the mean, and is a result of the a much closer agreement between the two temperatures at very low ambient temperatures (< 268 Kelvin). It is not clear why these low temperature points do not follow a similar trend to the majority at higher ambient temperatures.

Given that all of the cloud cameras are of a similar design, it may be reasonable to assume that the temperature of the chopper wheel T_{chop} is (in degrees Celsius or Kelvin):

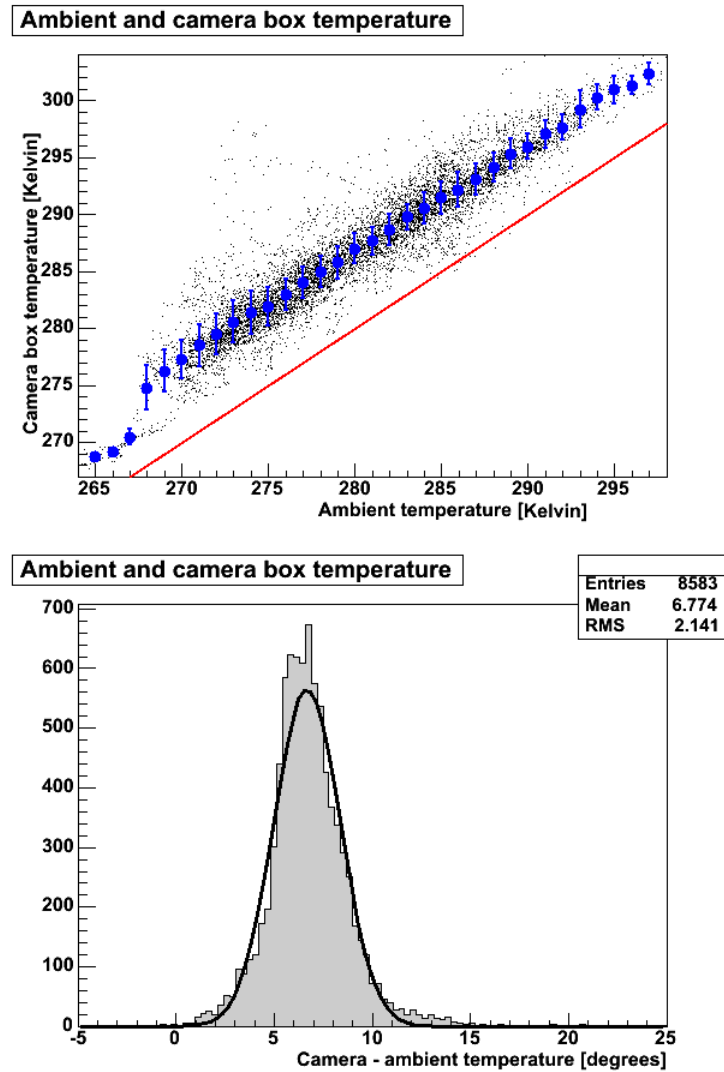$$T_{chop} = (T_{ambient} + 6.8) \pm 2.1 \tag{3.23}$$

Figure 3.11: *Ambient and Loma Amarilla cloud camera box temperatures recorded between October 2007 and September 2008. Ambient temperature refers to the average of all available ambient temperature measurements.* **[Top]** *Black markers indicate a measured camera box temperature and its associated ambient temperature measurement, the red line indicates where the two measurements would be equal and the blue marks with error bars are the mean camera box temperatures and their standard deviation.* **[Bottom]** *A histogram representing differences between the ambient and camera box temperature measurements, with the thick line representing the form of a fitted Gaussian function.*

where 2.1 is the standard deviation of the approximation.

3.4.1 Clear night sky signal

According to equation 3.19, for a section of clear night sky the signal (S) measured by an infrared camera pixel can be parameterized by an equation of form:

$$S = A + B.T_{clear}.x + C.T_{clear}.x^2 + D.T_{clear}.x^3 + ... \qquad (3.24)$$

where A, B, C and D are fitted parameters, $x = (T_{chop}^4 - T_{clear}^4)/T_{clear}^4$, and T_{chop} and T_{clear} are the effective temperatures of the chopper and clear night sky respectively.

A single pixel radiometric thermopile installed with the Loma Amarilla camera allows this hypothesis to be tested. This radiometer measures the flux of incident infrared light between 5.5-20μm and outputs a voltage proportional to the scene temperature. This output voltage has been calibrated experimentally to report an effective blackbody temperature for whatever object the thermopile is studying.

Infrared images recorded by the Loma Amarilla camera directly above the fluorescence detector (for construction of the 27 image mosaics) were gathered for the period between the beginning of October 2007 and the end of September 2008, along with temperatures recorded by the attached thermopile. Measurements of cloud fraction made by LIDARs were used to identify images thought to be completely free of cloud. The temperature within the Loma Amarilla cloud camera box is measured directly by instrumentation within the box.

Out of the 8583 images gathered for the study, 980 were identified as being completely free of cloud. The signal within the central 16 pixels (the attach thermopile measures the sky within this region) was averaged to give a camera signal measurement which was then associated with sky temperature measurements by the thermopile, and temperature measurements within the camera box. These signals were fitted to various parameterizations suggested by equation 3.24 and the RMS of the fit recorded within table 3.1.

As expected, those parameterizations which contain the higher order terms perform better (with a lower RMS) than those that only contain lower order ones. Higher order polynomials will naturally fit the data better than lower order ones however, therefore it is difficult to appreciate whether the decrease in RMS is as a result of better approximating equation 3.20, or simply because there are more parameters available to be fitted.

Another possible fit takes the form of equation 3.25:

$$S = A + B(T_{box}^4 - T_{clear}^4) \qquad (3.25)$$

Form of fit	RMS of fit
$S = a + bT_{clear}x$	242
$S = a + bT_{clear}x + cT_{clear}x^2$	241
$S = a + bT_{clear}x + cT_{clear}x^2 + dT_{clear}x^3$	231
$S = a + bT_{clear}x + cT_{clear}x^2 + dT_{clear}x^3 + eT_{clear}x^4$	214
$S = a + bT_{clear}x + cT_{clear}x^2 + dT_{clear}x^3 + eT_{clear}x^4 + fT_{clear}x^5$	209

Table 3.1: *Table showing different parameterizations tried and the RMS associated with that fit. a, b, c etc. are the fitted parameters.*

A fit of this form performs remarkably well with an RMS fit of 217 ($A = 16488$ and $B = -2.3\text{x}10^{-6}$), though this is not predicted by the toy model suggested in the previous section. This is likely related to the approximation made in the toy model about a strictly linear relationship between pixel temperature and polarization. Regardless of model used, the fitted parameters will vary between different cloud cameras and different flat-field calibrations for an individual camera, therefore it must be derived uniquely after each camera calibration. Due to its simplicity, and its relatively good ability to fit the data, equation 3.25 will be favoured when fitting data.

Within equation 3.23 in the previous section it was suggested that the box temperature T_{box} might be estimated from the ambient temperature outside a cloud camera's box. As not all cameras have temperature monitors within their box it is useful to see if the ambient temperature may be used instead of a camera box temperature measurement. Consider an equation of form:

$$S_{clear} = A + B((T_{amb} + k)^4 - T_{clear}^4) \qquad (3.26)$$

fitted to the clear sky data. Where A and B are fitted parameters and T_{box} is estimated by $T_{amb} + k$. A k-value of 0 implies that the chopper temperature is taken to be the same as the ambient temperature outside the box, while a non-zero value of k implies a consistent systematic offset of k degrees between the outside ambient temperature and chopper temperature.

The effectiveness of estimating the box temperature T_{box} as the ambient temperature with some constant offset is examined in figure 3.12. The RMS of a linear fit to clear sky camera signals using the parameterization in equation 3.26 is shown, and is a measure of the success of the parameterization with respect to the goodness-of-fit achieved using the real T_{box} measurement. There is minimal difference of the fitted RMS using the '$T_{chop} = T_{amb} + k$' with varying amounts of k, with the RMS varying only slightly around the 263 range.
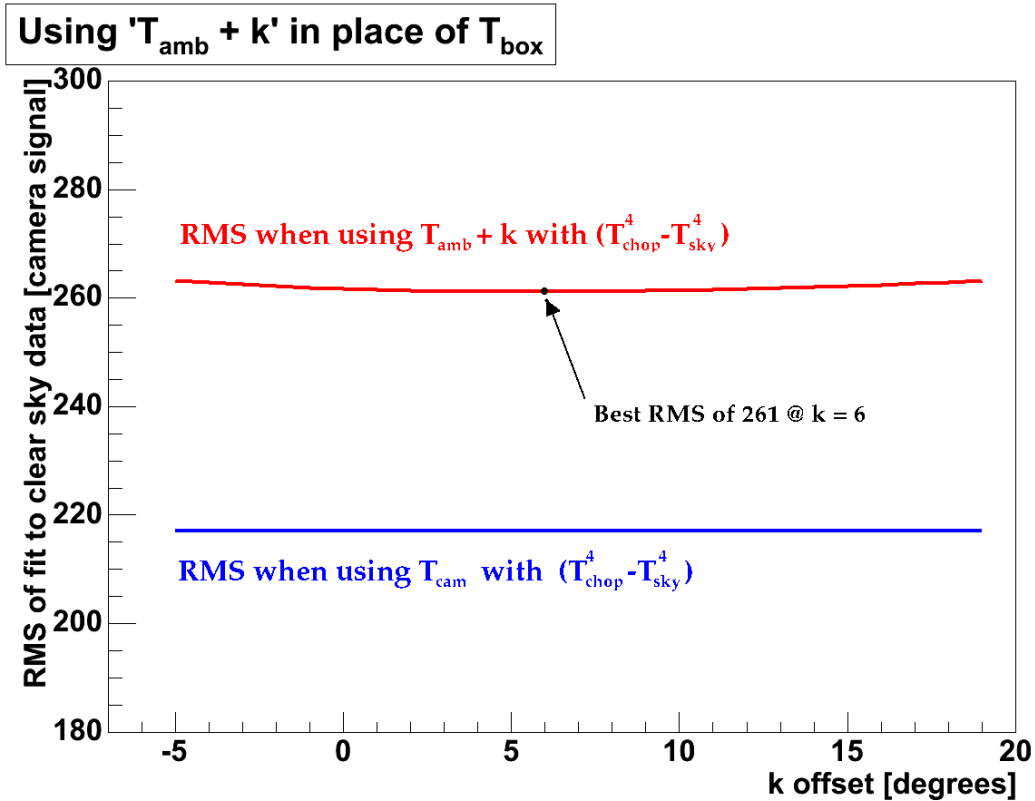
Using 'T$_{amb}$ + k' in place of T$_{box}$

RMS when using T$_{amb}$ + k with (T$_{chop}^{4}$-T$_{sky}^{4}$)

Best RMS of 261 @ k = 6

RMS when using T$_{cam}$ with (T$_{chop}^{4}$-T$_{sky}^{4}$)

Figure 3.12: *Plot showing the RMS of a fitted linear function to clear sky cloud camera data using the ambient temperature with an offset 'k' to estimate the camera's chopper temperature. Blue lines represent the RMS calculated using T_{cam} as T_{chop} and the red line using 'T$_{amb}$ + k' as T_{chop}.*

The goodness-of-fit achieved with use of the true T_{box} temperature is not matched through the use of any value of k, indicating that using this method of estimating the chopper temperature is not as effective as the direct use of the camera box temperature. As suggested by equation 3.23 however, the best RMS was found using a k-offset of around 6. The inability of any particular k-offset value to achieve the RMS achieved through the use of the internal camera temperatures is likely due to the internal camera temperature not just depending upon the external ambient temperature, but other factors as well. To maximize of the quality of any parameterizations created, a direct measurement of the box temperature T_{box} is therefore required, or a better way of estimating chopper or box temperature.

3.4.2   Cloudy sky signal

For a section of cloudy night sky, the radiation reaching the cloud camera is a combination of that from the gases in the atmosphere and that from the cloud itself. Following the form of the parameterization described in equation 3.25, the equation to be fitted for cloudy conditions becomes equation 3.27 below.

$$S = A + B(T_{chop}^4 - T_{clear}^4 - T_{cloud}^4) \qquad (3.27)$$

where T_{cloud} is the temperature of the cloud.

Using the Loma Amarilla's cloud camera's single pixel thermopile, this relationship will be examined much like the clear night sky was in the previous section. Loma Amarilla cloud camera images taken at the zenith angle were gathered from a period spanning October 2007 to September 2008, along with associated temperature and LIDAR cloud information. LIDAR cloud fraction measurements ($\geq 90\%$ cloud coverage) identified 991 overcast images within this set of images. The sky temperature measured by the attached thermopile in this case is equivalent to $\sqrt[4]{T_{clear}^4 + T_{cloud}^4}$, therefore a linear correlation between the chopper temperature (to the 4th power), thermopile measured sky temperature (to the 4th power) and cloud camera signal is expected.

Figure 3.13 demonstrates a linear fit of $(T_{chop}^4 - T_{clear}^4 - T_{cloud}^4)$ to cloud camera signal of the form:

$$S_{cloudy} = -4.89\mathrm{x}10^{-6}(T_{box}^4 - T_{clear}^4 - T_{cloud}^4) + 20872 \qquad (3.28)$$

with a fitted RMS of 653. This is a poorer fit than for the clear night sky in the previous section likely due to the sometimes non-isothermal structure of cloud (multiple cloud layers, small breaks in cloud cover etc), which complicate the signal further. As with the clear sky parameterization in the previous section, the fitted parameters will vary between different cloud cameras and after a particular camera has been flat-fielded.

Unfortunately the effective temperature of the cloud is difficult to estimate, due to uncertainty in cloud height, temperature lapse rate, cloud emissivities and attenuation effects. Thus equation 3.28 is not readily applicable to the majority of cloud camera data. Identification of 'cloudy' signals is perhaps best achieved by comparing a measured signal against the theoretical expectation for a clear signal under particular weather conditions, as demonstrated in figure 3.14. All the measurements from the Loma Amarilla sample of data (whether clear or cloudy) are shown with T_{chop} being estimated as '$T_{amb} + 6.8$' from equation 3.23 and T_{sky} from Maghrabi's Auger clear sky parameterization [130] in equation 3.29:

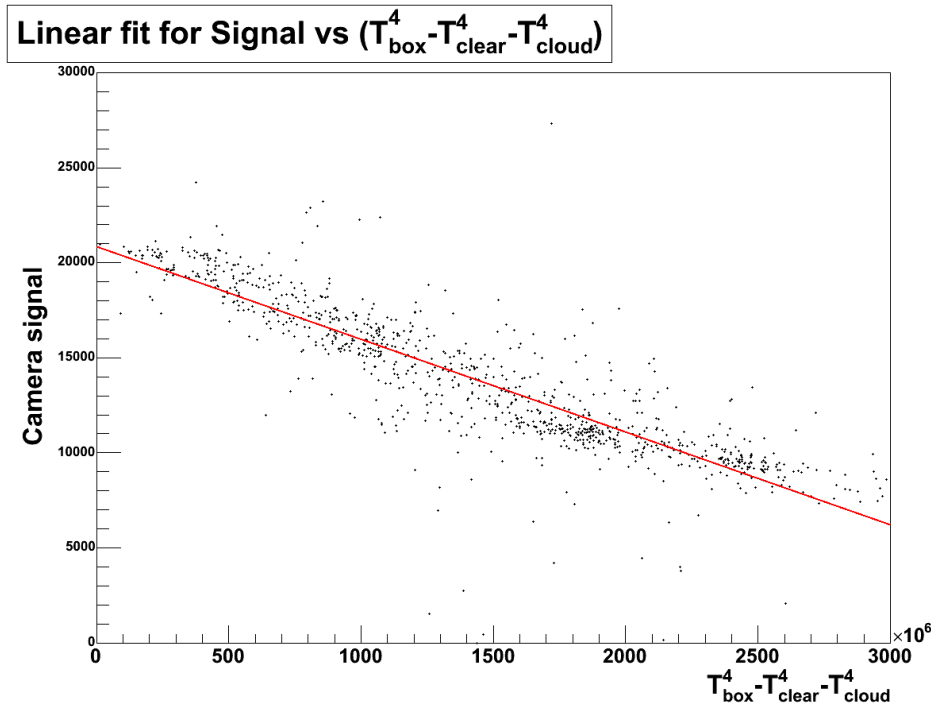$$T_{clear} = -45.59 + 8.05\sqrt{\epsilon_0} + 0.56T_{ambient} \qquad (3.29)$$

Figure 3.13: *Linear fit to overcast sky data using measured values of $(T_{box}^4 - T_{clear}^4 - T_{cloud}^4)$. Red line indicates the fitted straight line and black points indicate the camera signals associated with particular temperatures.*

where $T_{ambient}$ is the ambient temperature in degrees Celsius and ϵ_0 is the water vapor pressure in mb.

The blue line in figure 3.14 represents the theoretical expectation (according to equation 3.25) of clear sky signal. Measured points close to the line are expected to be more likely to be clear sky than cloud. Red marks indicate those measurements suggested by the LIDAR to be overcast, and hence are expected to differ from the blue clear sky expectation. Most of the overcast measurements agree with this expectation. Those measurements that don't are likely due to erronous identification by the LIDAR (LIDAR measurements were used from the other fluorescence detector sites) or because the cloud is so high (thus having a very low temperature) that the contribution is neglible against the clear sky background radiance.

Figure 3.15 shows the cloud heights measured during the overcast measurements (the red dots) in figure 3.14, and the square of the signal difference between the actual measurement and clear sky expectation. Most of the overcast measurements with low variance are of a higher altitude than
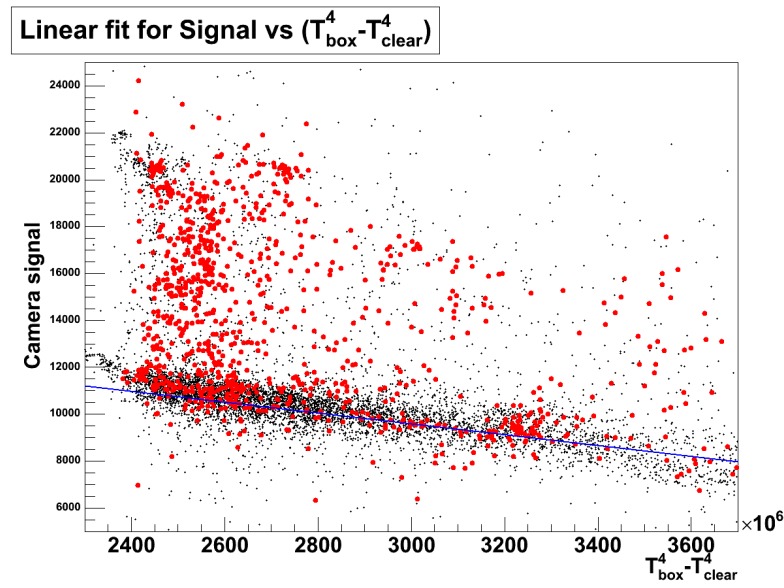
Figure 3.14: *Showing measured and predicted signals vs $(T_{chop}^4 - T_{clear}^4)$. Black dots are all measurements, red dots indicate measurements thought by LIDAR to be taken on overcast nights. The blue line indicates the theoretical expectation for clear sky signal by equation 3.25.*
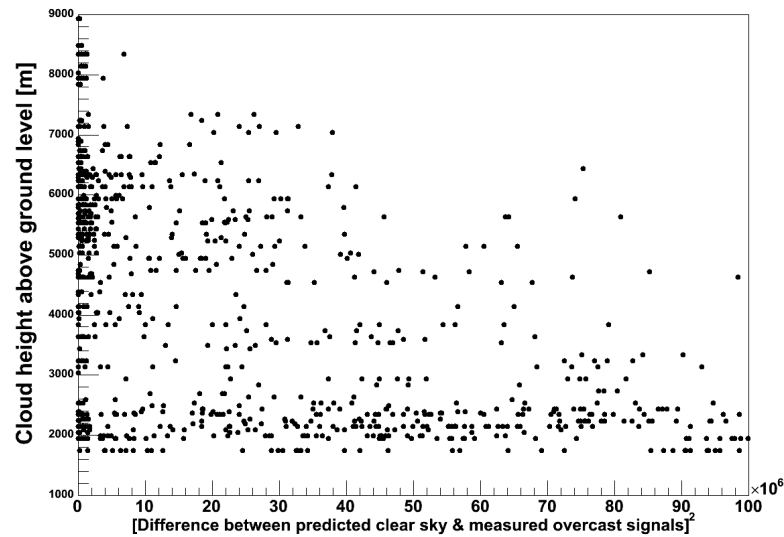

Figure 3.15: *Demonstrates the difference between measured overcast signals (red marks in figure 3.14) and the lowest cloud height measurement at the time.*

that of those of the greater variance. Those measurements with little variance and relatively low measured cloud heights, are likely measurements that have been mis-identified as being cloud.

3.4.3   Estimating scene temperature

With a parameterization of the form of equation 3.30 it is possible to estimate the actual effective temperature being observed by a particular pixel.

$$S = A + B \left(T_{chop}^4 - T_{sky}^4 \right) \tag{3.30}$$

where S is the signal output from a camera pixel, T_{chop} and T_{sky} are the temperatures of the chopper and sky respectively, and A and B are the fitted parameters.

The radiometer attached to the Loma Amarilla cloud camera allows a parameterization for signal as a function of actual sky temperature and chopper temperature to be created. Two months worth of data from the Loma Amarilla cloud camera in November and December 2007 was assembled and the signal recorded by the camera and the corresponding sky temperature measured by the attached thermopile recorded. The result may be seen in figure 3.16. Different data points are marked in black, while LIDAR identified clear sky and cloudy measurements were used to fit equation 3.30 as the blue and red lines respectively.

The fits are different due to the difference in radiation bandwidth being received by both the radiometer and the infrared camera, and the fact that clouds radiate as a blackbody. The camera samples radiation in the range 7.5-13 μm, while the thermopile samples in the range 5.5-20 μm. As seen in figure 3.5, a black body radiation spectrum is observed for non-cirrus clouds, and a non-black body spectrum is observed for clear sky and cirrus clouds. Given their different bandwidths, each instrument is going to be faced with a different proportional change in light intensity between clear, and cloud conditions. Therefore the radiometer and the cloud camera are going to have a different response while viewing clear and cloudy conditions.

It makes sense to calibrate the cameras to estimate temperature based upon effective blackbody temperature, therefore it is obvious to fit the equation 3.30 parameterization using overcast blackbody cloud data, and use that as an estimation of temperature, as seen in equation 3.31. The fit for overcast cloud conditions is not as good as for clear sky conditions however, therefore in the interest of precision it may be better to fit using only clear sky data.

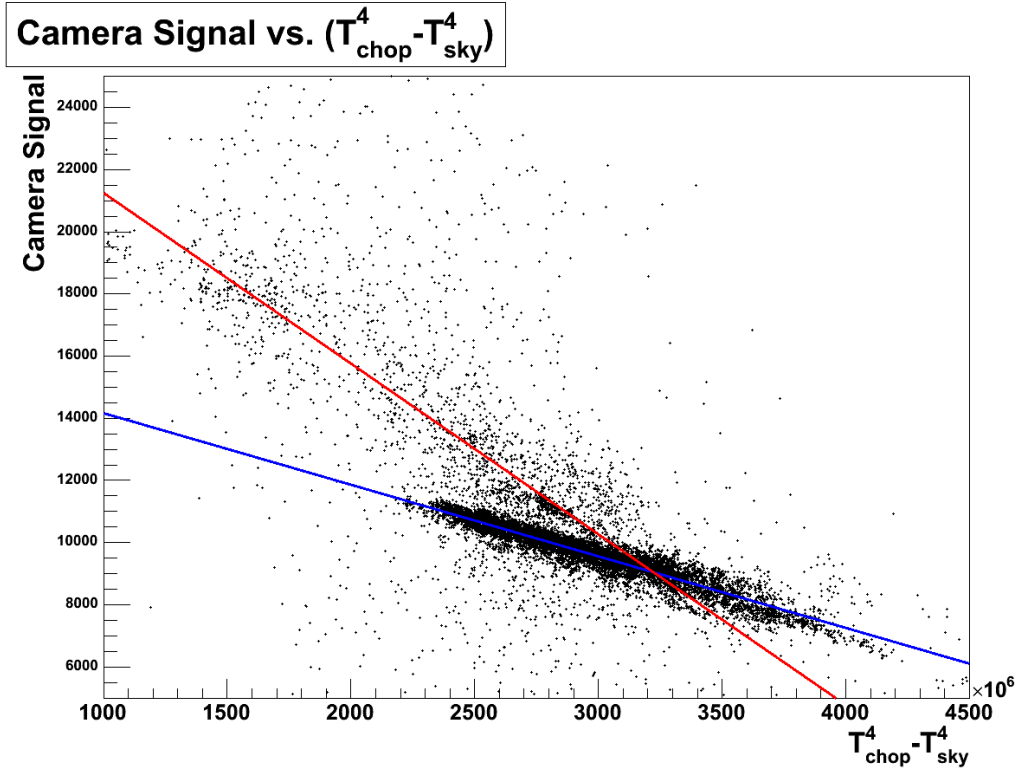$$T_{sky} = \sqrt[4]{T_{chop}^4 - \frac{S - A}{B}} \tag{3.31}$$

Figure 3.16: *Plot showing the signal recorded by the Loma Amarilla cloud camera, and the corresponding ($T_{chop}^4 - T_{sky}^4$) measurement made by the attached radiometer. The red line indicates the fit made by equation 3.30 to cloudy signals (identified by the LIDAR), and the blue indicates a fit made to clear sky signals, also identified by the LIDAR.*

      Figure 3.17 shows the residuals in estimating temperature as a function of signal and chopper temperature using equation 3.31 with the parameters A and B estimated using equation 3.30. The parameterization fitted with clear sky data manages to estimate the radiometer measured temperature with an RMS uncertainty of around 2°C, and the cloudy based parameterization with an RMS uncertainty of around 6°C. Such parameterizations must be calculated for each individual camera, and must be recalculated when that camera undergoes a flat fielding calibration.

      From the standpoint of calibrating the Loma Amarilla cloud camera to estimate the effective black body temperature of an object with the radiometer, it makes sense to use overcast cloud conditions, as they best represent an actual black body. Such a calibration has a much higher de-
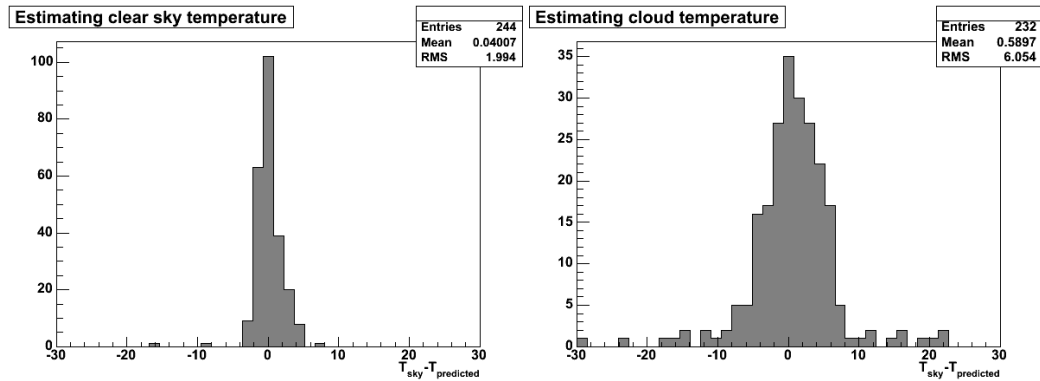
Figure 3.17: *Histograms of differences between radiometer measured temperature T_{sky} and estimated temperature $T_{predicted}$, obtained through fitting equation 3.30 and then using equation 3.31.*

gree of uncertainty than that based upon clear sky conditions however. Due to the different band widths of the radiometer and the cloud camera, clear sky conditions evoke a different response in the two instruments, making it technically incorrect to use as a black body temperature calibration.

The precision with which the clear sky temperature was able to be predicted suggests that it would be possible to work out a good estimation of temperature from the cloud camera signal and chopper temperature. A calibrated radiometer with the same bandpass as the cloud cameras would allow such a calibration to take place, as the less erratic clear night sky data would then be able to be used in the fitting process. For cameras without an attached radiometer, it may be possible to use the predictions of the effective blackbody temperature of the clear night sky (using ground measured parameters such as water vapor pressure and ambient temperature) to calibrate the cloud cameras.

3.5 Camera image artifacts

There are several hardware induced image artifacts or anomalies that may sometimes be observed, which occasionally interfere with analysis of the cloud camera images. Firstly is the aural effect, whereby dark and bright auras appear around the boundary between hot and cold objects - further emphasizing their contrast. Secondly is a series of streaking bands of fluctuating intensity across the image. Lastly is barrel distortion appearing in all images whereby the image as a whole appears to be slightly warped around its edges.

3.5.1   Aural effect

One of the most common (and useful!) artifacts observed in the cloud cameras are the auras. The aural effect takes the form of dark and bright bands at the boundaries between objects of differing temperature within the camera's field-of-view. This is a direct result of the scene differencing process used to exploit the pyroelectric effect used in camera operation. While often appearing within images, this effect rarely causes a concern, and is often quite beneficial as the aura adds extra emphasis to the boundaries between objects of differing temperature - such as clouds and clear night sky.

Within the Raytheon IR cameras, auras appear as regions of extra brightness and darkness around any boundary between two objects of greatly differing temperature. The lower temperature object will have a dark area at the boundary, and the higher temperature object will appear much brighter than it otherwise would at the boundary. This effect may be observed in the bottom two images in figure 3.18.

Auras appear due to the image differencing effect used in these particular cameras. The signal output by each pixel is approximately proportional to the difference between the temperatures (to the 4th power) of whatever its looking at, and the apparent temperature of the scene while looking through the diffusing Germanium chopper wheel. If a particular pixel happens to be looking at a region of low temperature, with a hot region nearby (and so hence a high scene average temperature), then the differencing process will result in a small signal which takes the form of a dark aura. The opposite situation applies for the brighter aura. The process is demonstrated in figure 3.18 where a diffused image of the top left image is created through a Gaussian filter and is then subtracted from the original image - approximately imitating the action of the camera. Dark and light auras can be clearly seen in both the artificially created image and in the actual cloud camera image within the figure.

This effect is useful in the case of the cloud cameras because it can emphasize the presence of clouds in the night sky. The auras not only make the clouds appear brighter, but it also darken out the clear night sky. Edge detection algorithms are also aided by this effect, as the gradient separating the cloud from clear sky is increased in magnitude. This effect is not always evident, as may be seen in some of the more distant clouds in the bottom right image in figure 3.18, likely due to the lesser contrast between cloud and clear sky.
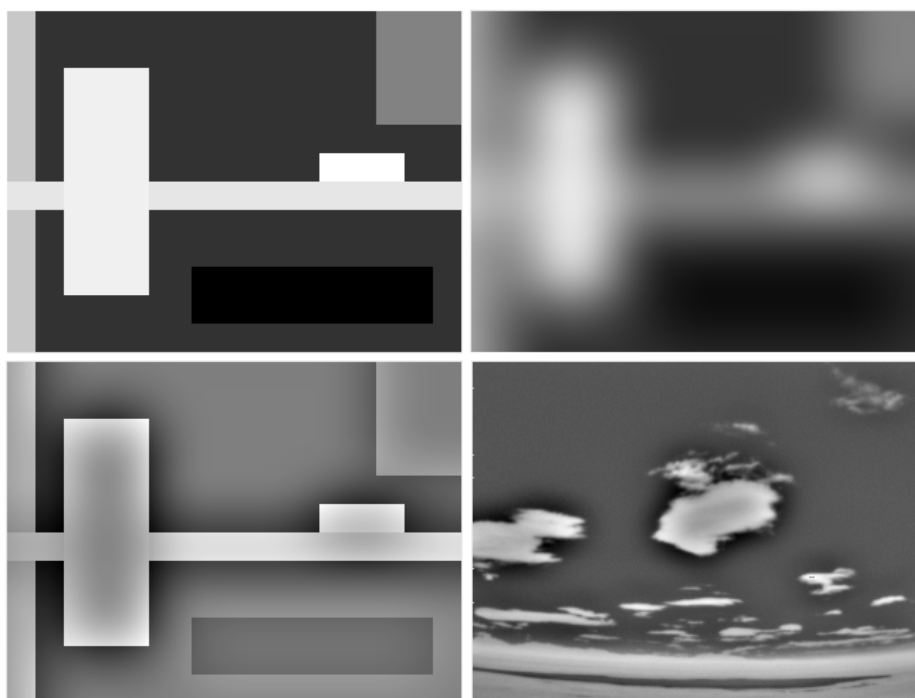
Figure 3.18: **[Top left]** *A set of rectangles with different 'infrared intensities', representing a scene a cloud camera is looking at without looking through the Germanium chopper wheel.* **[Top right]** *A gaussian filtered version of the top left image, representing what a cloud camera might see looking through the Germanium chopper wheel.* **[Bottom left]** *Is the normalized difference between the two top images, representing the image recorded by a cloud camera.* **[Bottom right]** *An actual picture taken of some clouds by a cloud camera.*

3.5.2 Streaking

Streaking is an image artifact that occurs in some cameras when viewing an isothermal scene - such as a very overcast or clear night sky. It appears as a series of circular streaks of modulating intensity across the image. This effect is thought to be the result of a mis-aligned chopper edge within the cloud camera. This artifact is easy enough to spot and overcome with manual inspection, however it often interferes with a more automated cloud detection attempt.

When several circular streaks of dark and light bands across a cloud camera image appear, this effect is called of streaking. It usually only becomes apparent when viewing a very isothermal scene on either very overcast or clear nights and is difficult to detect in more complicated non-isothermal
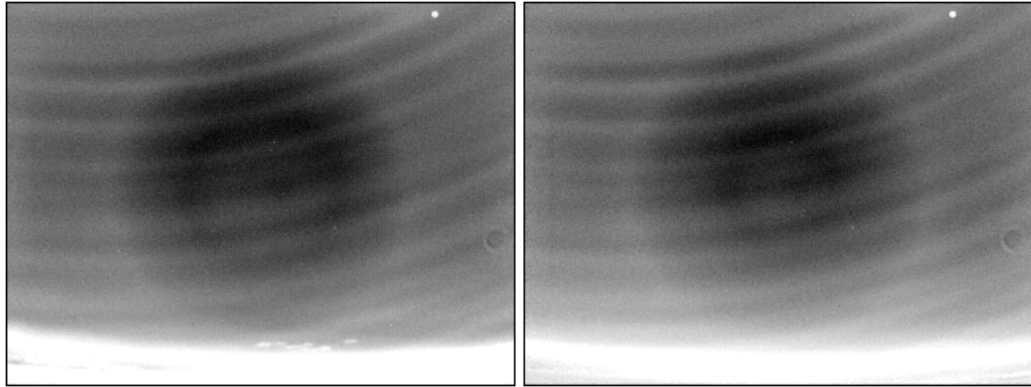
Figure 3.19:   *Two images taken by the Coihueco cloud camera. Examples of image streaking (the radial circular dark/light bands coming down from the top left-hand side of the image).*

scenes. Some examples of the effect may be seen in figure 3.19, where the horizontally curving bands of modulating intensity are the effect of interest. The apparent intensity of the streaks is strong enough to be readily apparent to the human eye, though the lack of texture in the night sky and the immobile nature of the streaks over the course of several sets of images allows identification of the streaks as a camera artefact and not cloud.

Streaking is a hardware induced artifact and is thought to be the result of a mis-aligned chopper edge within the camera itself. The camera samples the signal from each pixel twice per cycle, once just before a pixel is obscured by the chopper wheel and again just before a pixel is released from the chopper obscuration. The chopper itself uses an Archimedean spiral pattern (see section 3.3.1) to approximate a straight chopper edge moving across the pixel array at a constant speed. The speed of this 'straight' chopper edge varies with distance from the center. For the effective vertical speed $\frac{dy}{dt}$ of the 'straight edge' chopper along an axis, see equation 3.32:

$$\frac{dy}{dt} = \frac{d\theta}{dt}(a - x) \tag{3.32}$$

where $\frac{d\theta}{dt}$ is the rotational speed of the chopper, a is the constant in the Archimedes spiral pattern and x is the distance being considered perpendicular to the 'vertically' moving direction, thus the effective edge of the chopper is actually curved as is demonstrated in figure 3.20.

This means that different pixels are being sampled at different times during their heating and cooling cycles. The signal output of a pixel depends
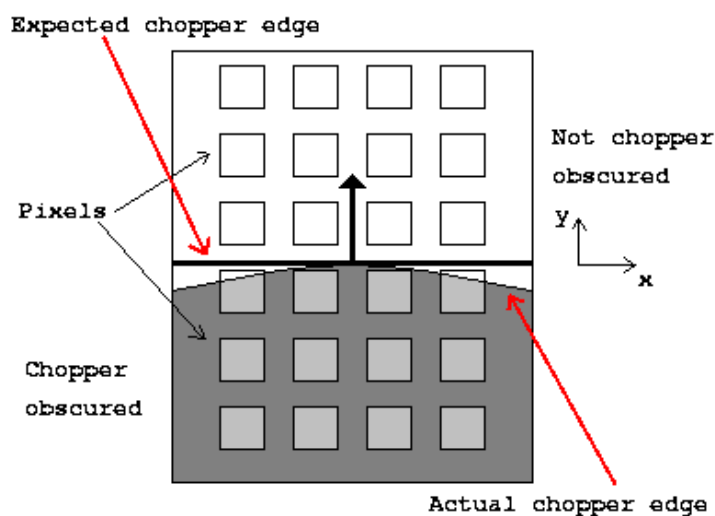
Figure 3.20: *A diagram showing an imperfection in the chopper wheel (moving to the right) that may lead to streaking in images. Grey represents regions that are blocked by the Germanium chopper.*

on the rate-of-change ($\frac{dT}{dt}$) of temperature with time (see subsection 3.4) and $\frac{dT}{dt}$ is non-linear - therefore for a given scene each pixel will have a slightly different gain induced by the relative position of chopper when it is being sampled. As this gain is non-linear it is not fully accounted for by the camera normalization process. The multiple bands occur as the effective straight edge moves closer, then further away from its theoretical position as a function of distance from the centre of the camera - inducing a spatially modulated change in gain.

The streaking is only evident in very isothermal scenes such as very clear or overcast nights. This is because in reality the effect is only very small and is only readily apparent in isothermal conditions where there is little signal being registered by the pixels normally (since the scene temperature and scene average temperatures are relatively similar). In terms of image processing, streaking may sometimes appear to be very fine, high altitude cloud due to the gradients in the image created by this effect, thus sometimes resulting in incorrect analysis by an automated processing attempt. The effect is usually easy to spot and correct by a human operator however as identical streaks will appear in multiple sequential images.

3.5.3   Barrel distortion

All four of the cloud cameras suffer from barrel distortion, which must be
accounted for to accurately correlate measurements by the cloud cameras
with pixels within the fluorescence detector. Barrel distortion is an optical
effect common in cameras with large fields of view, whereby a recorded image
is distorted in such a fashion that any straight lines within the image appear
to be curving away from the center of the image. The magnitude of the
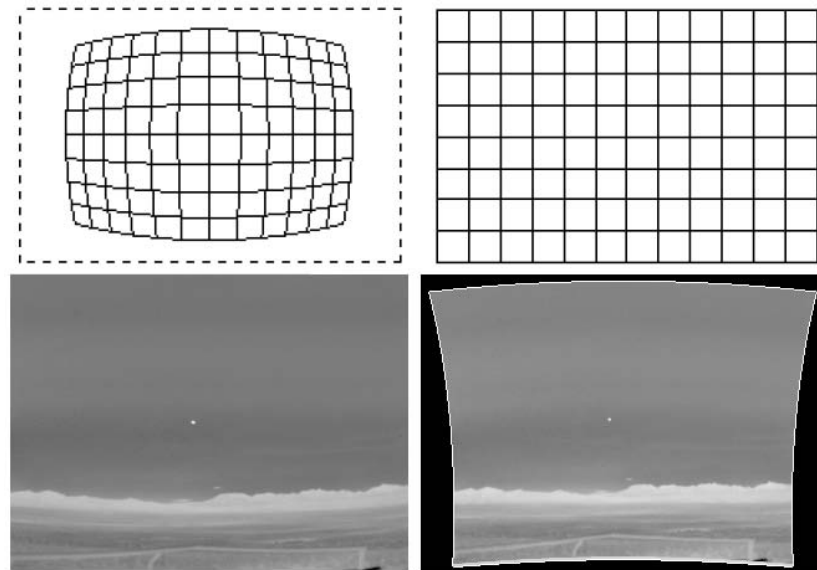distortion varies slightly within each camera but is correctable.

Figure 3.21: *[**Top**] Diagrams representing the shape of the distortion (or lack
thereof) of the images below.* [**Bottom left**] *An image recorded by a cloud camera.*
[**Bottom right**] *Same as image on the left but with its barrel distortion corrected.*

Barrel distortion is the result of light from an image being focussed
on the image plane closer to the image center than it should otherwise be
(see figure 3.21). Any straight lines not running through the image center
will appear to be bent in towards the center of the image. Circular objects
centered in the image will not appear to be distorted, however their radius
will appear to have changed. The magnitude of the distortion varies with
distance from optical axis as seen in equation 3.33:

$$h_{seen} = h + a.h^3 + b.h^5 + ... \tag{3.33}$$

where h_{seen} is the observed distance from the optical axis (image center),
h is the real distance from image center and a/b/etc are constants unique

to the optical system. Note that barrel distortion is not a linear effect, the magnitude of its effect increases at larger distances from image center, and while the majority of the time the cubic term is the dominant non-linear term, there do exist some optical systems whereby the higher order coefficients (b/etc) are large enough to outweigh the cubic one.

If $a > 0$ in equation 3.33, barrel distortion occurs. If $a < 0$ however, then pin-cushion distortion occurs, and any vertical or horizontal straight lines not running through image center will appear to be curving away from the center of the image. Only barrel distortion seems to occur within the cloud cameras.

Correction of barrel distortion within the cloud cameras is the result of work carried out by Dr Andrew Smith at Adelaide University and involves the use of equation 3.33. Equation 3.33 may be re-written into equation 3.34 using a reversion of series [15]:

$$h = h_{seen} + a_1.h_{seen}^3 + b_1.h_{seen}^5 + ... \qquad (3.34)$$

where a_1/b_1/etc are a new set of coefficients (to those in equation 3.33). Therefore correcting barrel distortion within an image is a simple matter of determining a_1/b_1/etc and mapping a new image using equation 3.34.

Working out the unknown coefficients may be done with guesswork (if there exists some way of testing the correctness of the barrel distortion correction), or through some alternate means. In the case of the cloud cameras, moon studies are carried out, whereby the position of the moon is tracked as it crosses the field of view of the cloud camera. As the actual position of the moon may be calculated, we may compare this to where it appears within the camera image. Coefficients within equation 3.34, may then be calculated and the cloud images corrected.